RICE UNIVERSITY

Electron Energy Loss Spectroscopy and Optical Properties of Plasmonic Nanostructure

by

Yang Cao

A THESIS SUBMITTED
IN PARTIAL FULFILLMENT OF THE
REQUIREMENTS FOR THE DEGREE

Doctor of Philosophy

APPROVED, THESIS COMMITTEE

Peter Nordlander, Chair
Wiess Chair and Professor of Physics and
Astronomy; Professor of Electrical and
Computer Engineering; Professor of
Materials Science and NanoEngineering

Frank Geurts
Assistant Professor of Physics and
Astronomy

Naomi Halas
Stanley C. Moore Professor in Electrical
and Computer Engineering; Professor of
Biomedical Engineering, Chemistry,
Physics and Astronomy; Director,
Laboratory for Nanophotonics

HOUSTON, TEXAS
April 2015

ABSTRACT

Electron Energy Loss Spectroscopy and Optical Properties of Plasmonic Nanostructure

by

Yang Cao

Plasmon is considered to be the incompressible self-oscillation of conducting electrons in small nanoparticles. A classical spring model could be used to describe plasmon's behavior. Many different techniques have been applied to understand nanostructure's plasmonic properties. Electron energy loss spectroscopy (EELS) is one of these tools, which is helpful for us to understand the interaction between fast moving electrons and nanomaterials. It could achieve very high spatial and energy resolution. Here, we develop a new finite-difference time-domain method to calculate EELS spectra and maps, which is based on a commercial software package "Lumerical". The calculated results for different cases are compared with the well-known boundary element method (BEM) and show an excellent agreement. Our finite-difference time-domain (FDTD) method to calculate EELS spectra has further been proven really helpful by high-density plasmonic dimers' experimental results.

There are basically two different numerical techniques. One is based on finite difference method (FEM) and another is according to finite-difference time-domain method (FDTD). Both of them are very important to perform optical calculations in

nanophotonics and plasmonics area. In general, they will try to solve Maxwell equations with many different boundary conditions numerically.

Optical properties of nanomaterials are also very tremendous for us to understand plasmonics behavior in the external electromagnetic fields. We systematically performed FEM simulations for different dimensions' split ring structure and identified each plasmon mode via induced charge plot. Later we also studied hollow Au Nanoshells: hollow Au-Ag Nanoshell and hollow Au-Co Nanoshell. The former showed the surprising in vivo instability in the near infrared region while the later has potential application in hot electron generation.

Acknowledgments

During my graduate research and study, I will thank all the people who give me a lot of help and inspire. First, I will thank to my supervisor, Dr. Peter Nordlander. Whenever I met with some challenging, he could always give me a lot of feasible suggestions during the weekly group meeting. These excellent strategies shown me a brand new road to go and explore, which made me full of energy and courage. Even though I got lost in a difficult project for a long time, he is always very patient and gives me a lot of credit for the endeavor I made. Besides, he is a very humorous, which makes the group meeting's atmosphere very comfortable and interesting. I am thankful to him who instructs me how to do the research and to collaborate with researchers in other group. At the meantime, I will also thank for my thesis committee members: Dr. Naomi Halas and Dr. Frank Geurts. Thank you so much to spend your tremendous valuable time to attend my PhD thesis defense. What's more, I would like to thank all the current and previous group members in our group: Dr. Yumin Wang, Dr. Ke Zhao, Dr. Nicolas Large, Dr. Alejandro Manjavacas, Dr. Lifei Liu, Dr. Kui Bao, Dr. Yang Li, Dr. Yurong Zhen, Dr. Chizuko Dutta, Dr. Hui Zhang, Dr. Vikram Kulkarni, Mr. Jun Liu, Mr. Hangqi Zhao, Ms. Yue Zhang, Mr. Xiao Yang, Mr. Thawda Aung. I will specially thank to Dr. Ke Zhao, who gave me tremendous theoretical instructions and supports for my first project. Also I would like to show my many thanks to Dr. Yumin Wang, who trained me to use a myriad of different numerical techniques and how to perform the debug in the coding and simulations during my following projects. Living and working with these members

in the group makes me feel more confident when dealing with difficulties and makes the life more colorful. Later, I will also thank to the Laboratory for Nanophotonics (LANP), which will hold a poster session once a month to enable us to know the latest and hottest research topics other great nanophotonics groups are doing. Also my thanks will go to other collaborators, Prof. Naomi Halas, Dr. Mark Knight, Ms. Amanda Goodman, Mr. Ali Sobhani, Ms. Christyn Thibodeaux, Prof. Paul Cremer, Dr. Yangjun Cai, Prof. Shan Wang, Dr. Mingliang Zhang. During these processes, I have learned how to collaborate efficiently with other people and known the importance of teamwork. Last but not the least; please allow me to express my deepest gratitude to my parents. Thank you for your support and love during my graduate life. Finally, I will also want to thank to all the funding agencies.

Contents

List of Figures

List of Tables

List of Equations

Nomenclature

EELS	Electron Energy Loss Spectroscopy
FDTD	Finite-Difference Time-Domain
FEM	Finite Element Method
BEM	Boundary Element Method
DDA	Discrete Dipole Approximation
PH	Plasmon Hybridization
MPI	Message Passing Interface
NIR	Near-Infrared
EMT	Effective Medium Theory
SCL	Stretchable Colloidal Lithography
EBL	Electron Beam Lithography
SRRs	Split-Ring Resonators
UV	Ultraviolet
RIE	Reactive Ion Etching
PML	Perfectly Matched Layer
MCMs	Multi-Coefficient Models
ppw	Points Per Wavelength
LSPR	Localized Surface Plasmon Resonance
SEM	Scanning Electron Microscopy
TEM	Transmission Electron Microscopy
STEM	Scanning Transmission Electron Microscopy

AFM	Atomic Force Microscopy
NIL	Nanoimprint Lithography
HAADF	High Angle Annular Dark Field
NRI	Negative Refractive Indices
FIB	Focused Ion Beam
ERs	Elliptical Rings
PS	Polystyrene
PDMS	Poly (dimethylsiloxane)
AR	Aspect Ratio
HGNS	Hollow Gold Nanoshells
PEG	Polyethyleneglycol
PTT	Photothermal Therapy
XPS	X-ray Photoelectron Spectroscopy
ICP-MS	Inductively Coupled Plasma Mass Spectrometry
FWHM	Full Width at Half Maximum

Chapter 1

Introduction

Plasmonics and nanophotonics have many interesting optical and electronic properties in current research area. Many different numerical techniques have been applied to simulate their optical reactions as shown in the experiment. These techniques may include: finite-difference time-domain method (FDTD), finite element method (FEM), boundary element method (BEM), discrete dipole approximation (DDA) etc. Regarding each method's advantage and disadvantage, both FDTD and FEM could solve arbitrary systems even without symmetry. However, FDTD restricts to Cartesian coordinates, which may meet with difficulties facing complicated geometries in some complex boundary conditions. The good thing for FDTD is that it could be implemented to run on the high performance-computing server via message passing interface (MPI). On the other hand, FEM is

more flexible in discretization. For instance, in three-dimensional space, it could not only use cube as basic element but also tetrahedron, hexahedra etc. These different discretization techniques will make it more convenient to solve such complex geometries. For BEM, it only discretizes two-dimensional surfaces. Besides these numerical methods mentioned above, there are also other analytical methods. Mie theory is one of the most important theoretical methods to deal with scattering and absorbing of light by small nanoparticles. Comparing with other numerical methods, Mie theory's calculation is much faster. To reach the same accuracy, Mie theory usually takes a few seconds. Nevertheless, it could only be used for spherical symmetrical systems.

Electron energy-loss spectroscopy (EELS) is one of the most important techniques used to detect plasmon's properties. By strong interaction between fast moving electrons and nanoparticle, the loss energy of electrons will be converted into nanostructure's plasmon energy, exciting different plasmon modes and enabling us to know more characteristics of certain nanomaterials. A lot of previous work and research has been put into calculating EELS spectra, such as DDA, FEM and so on. However, these methods have the following disadvantages: first, they couldn't solve the problem when electron beam penetrates the nanostructure; second, the system is often restricted to symmetrical one; third, supporting substrates effects often will be negligible. Here, we develop a novel technique to calculate EELS spectra and maps based on FDTD method. It could solve the penetrating case. At the meantime, the system we focused could have arbitrary geometry, not necessarily to be symmetric. This EELS-FDTD method has been implemented in a finite-difference

time-domain package and verified to be very useful and convenient for different cases. This technique has further been applied in the following case: high-density two-dimensional homo- and hetero- plasmonic dimers with universal sub-10-nm gaps. Great agreement between experimental and simulated EELS spectra further proved our new method's feasibility in real application.

Optical properties of nanomaterial are also very interesting to understand the interaction between photon and plasmonics. By using stretchable colloidal lithography (SCL), split-ring resonators (SRRs) have been fabricated in a very large scale. By calculating the optical spectra of SRRs, all of the different bright plasmon modes have been identified. Perfect agreement has been shown between UV-vis-NIR measurement and FEM calculations. By controlling O_2 RIE (Reactive ion etching) time, SRRs' dimension and gap distance could be changed. FEM calculations have also performed to see each of those parameters' influence. Finally, theoretical results show the same blue shift and intensity decreasing effects as shown in the experiments. Later, we also applied a simple standing-wave model to explain why SRRs could have so many and distinguished modes.

Nanomaterial has also a great application in bio-medical area. Hollow Au-Ag nanoshell is a very popular nanoparticle in cancel therapy area. By using Bruggeman effective medium theory (EMT), we have found the plasmon resonance peak would maintain at near-infrared(IR) region no matter how we change the particle's dimensions. Further FEM calculations have shown porosity plays a very important role controlling resonance peak's position. Besides, inhomogeneous broadening

seen in the transmission electron microscopy (TEM) is due to the porosity difference of each nanoshell in the ensemble. On the other hand, hollow Au-Co nanoshell could be used as a damping material. Here EMT has also been applied combined with Mie theory to discover the damping effects generated by Cobalt.

The thesis will be organized as follows: In Chapter 2, a novel EELS-FDTD method will be introduced. We will discuss about the theoretical formalism this method is based upon. Then we will talk about the configuration and model building in this finite-difference time-domain package. Later, we will compare different methods, such as BEM, DDA, Mie and EELS-FDTD and show the EESL-spectra. In order to further investigate different plasmon modes, we will also plot EELS-map's figure using EELS-FDTD method. Finally, we will also compare EELS-FDTD method with the experimental results on high-density plasmonic dimers' structure. In Chapter 3, a new fabrication technique called SCL will be introduced. We will talk about using this technique to fabricate SRRs in very large areas. Later, the optical spectra will be verified by FEM calculations. Mode analysis will also been mentioned to explain the meaning of peaks at different wavelength. In Chapter 4, EMT will be discussed in details regarding a mixture of different materials. FEM calculations will show that Au-Ag nanoshell's resonance can be maintain in the NIR region. Mie theory calculations support Cobalt will introduce damping factor in Au-Co nanoshell. In Chapter 5, the conclusion of the thesis will be made.

<div align="right">Chapter 2</div>

FDTD-EELS Method and Application

2.1. Introduction

Energy-loss spectroscopy could use many different kinds of particles to measure. Applying fast moving electrons is one of those techniques, which had been firstly used to detect surface plasmons in metals.[1–3] EELS could help us to reach a very high spatial resolution, which is less than 1 nm.[4,5] This is due to the fact that electron could be generated at a very high speed during the experiment, which is approximately half of the speed of light. So electron will have a very small de Broglie wavelength. Meanwhile, EELS would also achieve high energy resolution. In most cases, it is smaller than 0.1 eV.[6,7] EELS is a very important tool to detect all the plasmon modes, even if dark surface plasmon modes.[8–10] Therefore, EELS has been widely used to discover optical properties of very complicated nanostructures. A lot

of different EELS simulations have been worked out recently due to its popularity in the optical community, such as BEM,[11] FDTD,[12] FEM,[9] and DDA.[13] These methods could calculate EELS spectra and compare with the experimental results. However, many disadvantages may happen, such as non-penetrating cases,[13–15] symmetrical structures[13,14] and complex coding techniques.[12] So when met with some complex geometries in the experiments, such as asymmetrical structure with supported substrates, optical light excitation and near field calculation have been used to approximate EELS properties.[8,9,16,17] Here we provide a more robust and user-friendly method to simulate EELS spectra, called "EELS-FDTD".[18] This method is mainly based on a finite-difference time-domain software package "Lumerical".[19] It is very convenient even for those researchers who have less programming experiences.

2.2. Principle, theory and simulation set up

The nature of EELS theory has been extensively discussed in many papers.[1,4] Simple physical images could be considered as following: a fast moving electron beam will generate radiated electromagnetic field, which would polarize the nanostructures nearby. The polarized nanostructures will in turn generate induced field to prevent electron beam from moving. In this process, energy loss will be produced which would transfer to nanoparticle's plasmon energy according to the energy conservation principle. Basically, we could write the energy loss as the following mathematical form[4]

$$\Delta E_{EELS} = e \int \boldsymbol{v} \cdot \boldsymbol{E}^{ind}[\boldsymbol{r_e}(t), t]dt = \int_0^\infty \hbar\omega\Gamma_{EELS}(\omega)d\omega$$

Equation 2.1 – Electron energy loss.

Here, e is the electron charge unit, i.e. $1.602 \times 10^{-19}C$. $\boldsymbol{E}^{ind}$ is named the induced field, generated by the polarized nanostructure. $\boldsymbol{r_e}$ is electron's motion path vector. Γ_{EELS} could be calculated in the following way

$$\Gamma_{EELS}(\omega) = \frac{e}{\pi\hbar\omega}\int Re\{e^{-i\omega t}\boldsymbol{v} \cdot \boldsymbol{E}^{ind}[\boldsymbol{r_e}(t), \omega]\}dt + \Gamma_{bulk}(\omega)$$

Equation 2.2 – Energy loss probability.

It is called energy loss probability per unit of frequency ω.[4] Another term Γ_{bulk} on the right side of the equation is called bulk loss probability.[4] For the simplicity of the physics, we neglect bulk loss term. Meantime, any arbitrary current distribution could generate the following electric field[20]

$$\boldsymbol{E}[\boldsymbol{r}(t), \omega] = -4\pi i\omega \int \boldsymbol{G}(\boldsymbol{r}, \boldsymbol{r}', \omega)\boldsymbol{j}(\boldsymbol{r}', \omega)d\boldsymbol{r}'$$

Equation 2.3 – Generalized electric field by Green function

So we can treat generalized electric field as the integration of Green tensor in Maxwell's equations. More details could be got from solution of the following equation

$$\left[-\nabla \times \nabla \times +\varepsilon(\boldsymbol{r}, \omega)\frac{\omega^2}{c^2}\right]\boldsymbol{G}(\boldsymbol{r}, \boldsymbol{r}', \omega) = \frac{1}{c^2}\delta(\boldsymbol{r} - \boldsymbol{r}')\boldsymbol{I}$$

Equation 2.4 – Green tensor Maxwell's equation

Besides, we know electron current density could be written in the following way[4] (Here, we assume the electron beam travels in the x-z plane, perpendicular to x-axis. It has a distance of b away from the origin. We define this distance to be the impact parameter)

$$\boldsymbol{j}(\boldsymbol{r}', \omega) = -e\delta(x - b)\delta(y)e^{i\omega z/v}\hat{\boldsymbol{z}}$$

Equation 2.5 – Electron current density

So equation 2.2 could be further simplified as[4]

$$\Gamma_{EELS}(\omega) = \frac{4e^2}{\hbar}\iint_{-\infty}^{+\infty}\cos[\frac{\omega(z - z')}{v}] \times Im[-G_{zz}^{ind}(z, z', \omega)]dzdz'$$

Equation 2.6 – Energy loss probability written by Green function

What's more, Green tensor G_{zz}^{ind} has the following relationship with the z component of induced electric field E_z^{ind}

$$G_{zz}^{ind}(z, z', \omega) = -\frac{1}{4\pi\omega^2} \frac{E_z^{ind}(z, \omega)}{p(z', \omega)}$$

Equation 2.7 – Relation between induced Green tensor and induced field

With all of above, we could further write energy loss probability as

$$\Gamma_{EELS}(\omega) = \frac{e^2}{\pi\hbar\omega^2} \iint_{-\infty}^{+\infty} cos[\frac{\omega(z - z')}{v}] \times Im[\frac{E_z^{ind}(z, \omega)}{p(z', \omega)}] dz dz'$$

Equation 2.8 – Scalar form of energy loss probability in our configuration

In the formula above, we only need the imaginary part of induced field but no need of real part. In the finite-difference time-domain package, we just need to calculate the z component of induced electric field at each dipole source position. Detailed configuration could be seen in figure 2.1. Figure 2.1(a) schematically shows fast moving electron beam's field distribution. Figure 2.1 (b) illustrates total electric field's calculation when placing nanostructure with a distance of "b" away from electron beam. Figure 2.1 (c) tells background electric field's calculation by removing all the structures. Figure 2.1 (d) is the FDTD simulation configuration, showing the following items: (i) Simulation domain enclosed by perfectly matched layer (PML) (ii) Electric dipole source notation (In "Lumerical", dipole source is used to mimic electron beam's behavior) (iii) 1D monitor along z direction to record electric field's information (iv) Arbitrary nanostructure (v) Override mesh imposed on metallic nanostructure.
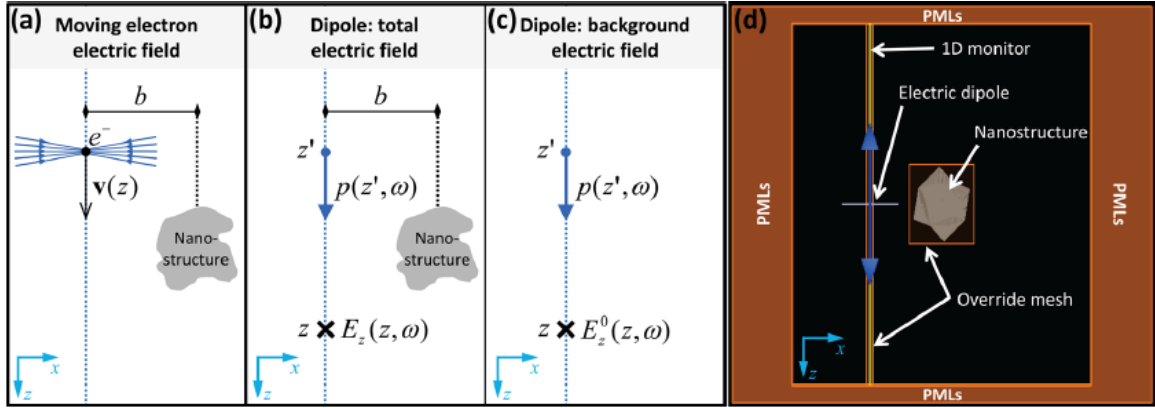
Figure 2.1 – Configuration to calculate EELS spectra.

If electron beam trajectory doesn't penetrate nanostructure, we only need to apply the total field to calculate EELS spectra instead of induced field. This is due to the fact that electron will not lose energy in the vacuum. However, in every case, we trend to use induced field to perform calculation because of FDTD's finite accuracy issue. Because of its user-friendly interface, we choose a commercial software "Lumerical" (Version 8.9.163) to perform electromagnetic field calculation based on classical Maxwell equation as following,[21]

$$\nabla \cdot \boldsymbol{E} = \frac{\rho}{\varepsilon_0}$$

$$\nabla \times \boldsymbol{E} = -\frac{\partial \boldsymbol{B}}{\partial t}$$

$$\nabla \cdot \boldsymbol{B} = 0$$

$$\nabla \times \boldsymbol{B} = \mu_0 \boldsymbol{J} + \mu_0 \varepsilon_0 \frac{\partial \boldsymbol{E}}{\partial t}$$

Equation 2.9 – Differential form of Maxwell equations in vacuum

The calculation started by setting a simulation domain box for 3D geometry. PML boundary conditions have been set in every direction to absorb all lights near the boundary.[22] At the meantime, we add an override mesh around the structures to further improve the numerical accuracy. Electric dipole has been put in every mesh grid point along electron's moving trajectory. Then we sweep electric dipole's position from bottom to top of the simulation box. For each dipole position, we use 1D monitor to record all the z component of electric field along electron's trajectory. In order to get the induced electric field, "two-steps" calculations have been provided according to figure 2.1 (b-c). Firstly total electric field has been calculated, and then we got the background electric field by getting rid of the samples. Finally, if we subtracted background electric field from total electric field, induced electric field could be obtained. For the special case when electron beam goes through nanostructure, we need to calculate background electric field by putting electric dipole in the medium full of nanostructure's materials. For example, if gold nanoparticle has been used, we need to calculate the electric field by putting dipole in the "sea" of bulk gold. However, if we do this in the real case, simulation will take forever since dispersive material goes beyond PML and numerical convergence becomes very slowly. Then if skin effects have been considered for perfect metal, we only need a finite volume of bulk metal to calculate the special background field. Due to the skin effects, electric field inside the metal will decay very quickly. As long as we get the induced field, we could calculate EELS spectra based on equation 2.8. This could be done in some post-processing stage.[18] Here, we applied 2D trapezoid numerical integration technique in MATLAB to get the results. There is also another

advantage using this EELS-FDTD method: if we meet with the same geometry except different electron beam energy, we could easily get each corresponding EELS spectra in the post-processing stage within seconds. Meanwhile, FDTD calculation has been paralleled in this software package, which will fasten our calculations greatly.

2.3. EELS-FDTD numerical results

We applied our EELS-FDTD method to the following different cases: (i) Non-coupling system (ii) Strongly coupled system (iii) System supported by substrates. Meantime, comparisons have been made between EELS-FDTD method with other well-known methods such as Mie theory and BEM method. Before we go into further details of numerical calculations, major materials dielectric functions will be shown in the figure 2.2 below. Figure 2.2 (a) dotted lines give both real and imaginary parts of gold obtained from experimental Johnson and Christy data.[23]
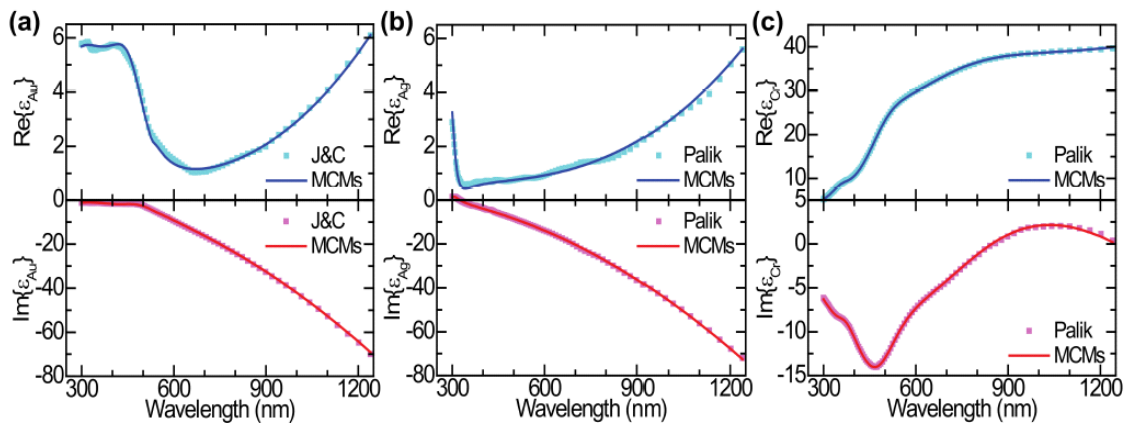
Figure 2.2 – Dielectric function of metals

Figure 2.2 (b) dotted lines show the dielectric function of silver obtained from Palik data.[24] Figure 2.2 (c) dotted lines show the dielectric function of chromium again obtained from Palik.[24] In all cases of figure 2.2 (a-c), solid lines are FDTD numerical fitting curves based on multi-coefficient models (MCMs). We could find excellent agreement between fitting curve and experimental tabulated data.

2.3.1. Non-coupling system
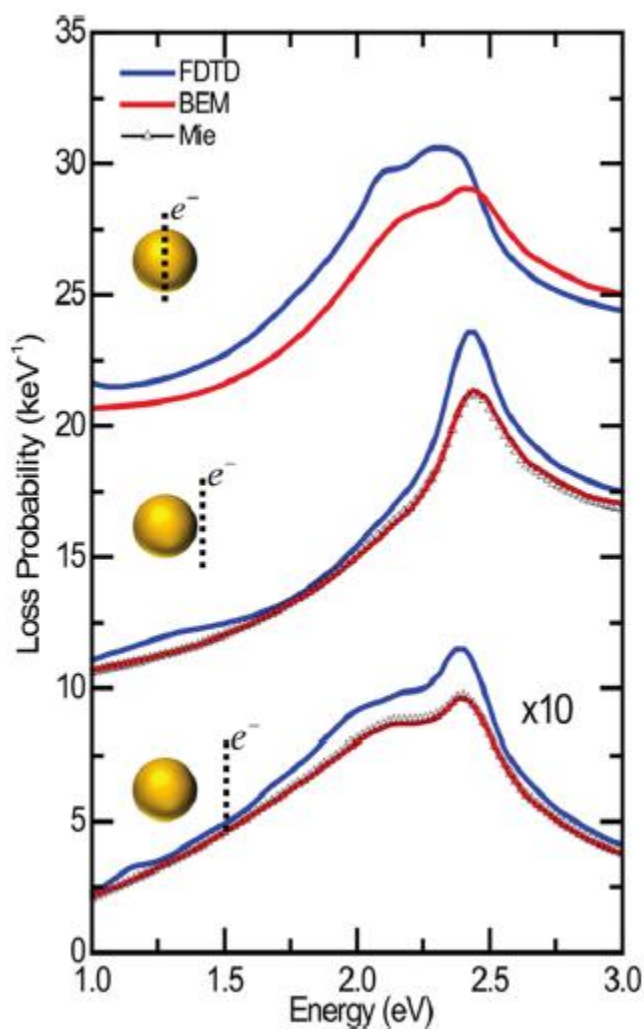
Figure 2.3 – Different methods EELS spectra for gold sphere

We consider the simplest case: single gold nanosphere in vacuum. The sphere's diameter is 160 nm. Johnson and Christy experimental data[23] has been used to model gold sphere's dielectric function. Besides, since this system is axial symmetric, BEM method could also be very convenient to implement. What's more, analytical Mie theory[25] could be applied to deal with spherical symmetric system. So we will compare three different numerical results: (i) FDTD (ii) BEM (iii) Mie, which could be seen in figure 2.3 above. However, when electron beam penetrates the gold sphere, Mie theory is not valid. Here we will focus on the novel FDTD method.
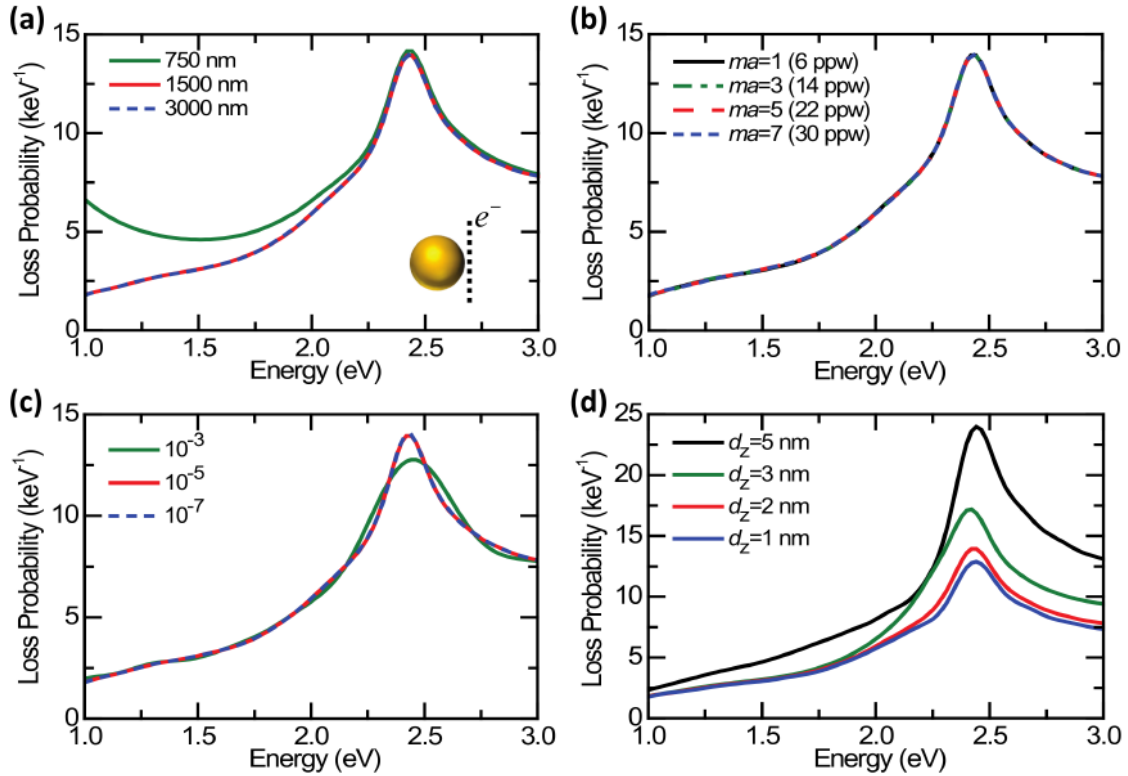
Figure 2.4 – Gold sphere EELS spectra's convergence test

Many convergence tests have been performed before the optimized parameters are found as shown in figure 2.4. Figure 2.4 (a) shows the simulation domain size and monitor's length effects, and we could see 1500 nm length of monitor is well enough to get converged result. Mesh accuracy is a discretized parameter to choose ranging from 1 to 8.[19] Mesh accuracy correlates to points per wavelength(ppw). If we want to simulate within an energy region e.g. 1~3 eV, wavelength mentioned above is the shortest value in that region. For instance, if mesh accuracy is 3, that means 14 points per wavelength used to do discretization in the space. Figure 2.4 (b) describes the result when changing the mesh accuracy. We could find mesh accuracy doesn't have a big effect on the spectra, meaning smaller mesh accuracy can be used to fasten our calculation. Auto shut-off parameter tells to stop the simulation when the total energy in the simulation domain falls to a significant small value.[19] The smaller value of auto shut-off, the better convergence result we can get. Figure 2.4 (c) illustrates that by using the auto shut-off parameter of 10^{-5}, we could already achieve a relative good convergent result. Figure 2.4 (d) shows the results by varying override mesh grid size. In the real application, we just need to use 2 nm to get relatively converged result within reasonable computational time.

Consider all of these different parameters' setting in Lumerical, we choose to use 1500 nm length of monitor to cover all of the electron trajectories. Mesh accuracy has been chosen to be "5" with the simulation time to be 100 femtosecond. Auto shut-off parameter is set to be 10^{-5}. Meantime, mesh refinement has been applied "Conformal variant 0". First, we calculate total electric field in the presence of gold nanosphere. In the second step, we calculate the background electric field by

removing the gold sphere. After that, induced electric field could be obtained. We sweep the wavelength from 400 nm to 1200 nm, corresponding to 1 eV to 3 eV. In figure 2.3, we calculate three different impact parameters: (i) b = 120 nm (ii) b = 82 nm (iii) b = 0 nm. For case (i), electron beam is quite far away from the sphere. In case (ii), electron beam is just 2 nm away from the boundary of the sphere. Finally, for case (iii), electron beam will penetrate the gold sphere. In all of the three cases mentioned above, electron's velocity is half of the speed of light, which means electron has energy of 80 keV.

From figure 2.3, we could see an excellent agreement between our FDTD method and BEM method. The latter one is almost the same as the analytical Mie theory's result. There is a major peak at the position of 2.4 eV and we identify it as the quadrupole mode of the gold nanoparticle. Besides, there is another less prominent shoulder mode at about 2.1 eV, corresponds to sphere's dipole mode. Since the particle's size is relatively large (Diameter is 160 nm), large retardation effects would be expected. That's the reason why peak position will shift when we change different impact parameters. Unlike some previous works[13–15,26] which have difficulty to deal with penetrating case, we could easily extend our FDTD method to tackle this problem. Nevertheless, we need to pay attention to the calculation of the background electric field, which will be in the bulk metal environment.

For the electron beam penetrates the sphere, we may also meet with the following numerical error: if we put the electric dipole at the exact interface between metal and vacuum, calculated EELS spectra based on FDTD will be overestimated

compared with BEM. From figure 2.5, we could find a very easy and quick solution to this issue. If we make the override mesh slightly different from case (i), mesh grid will not locate at the exact interface position. So in case (ii) and case (iii), EELS spectra are more close to BEM results.
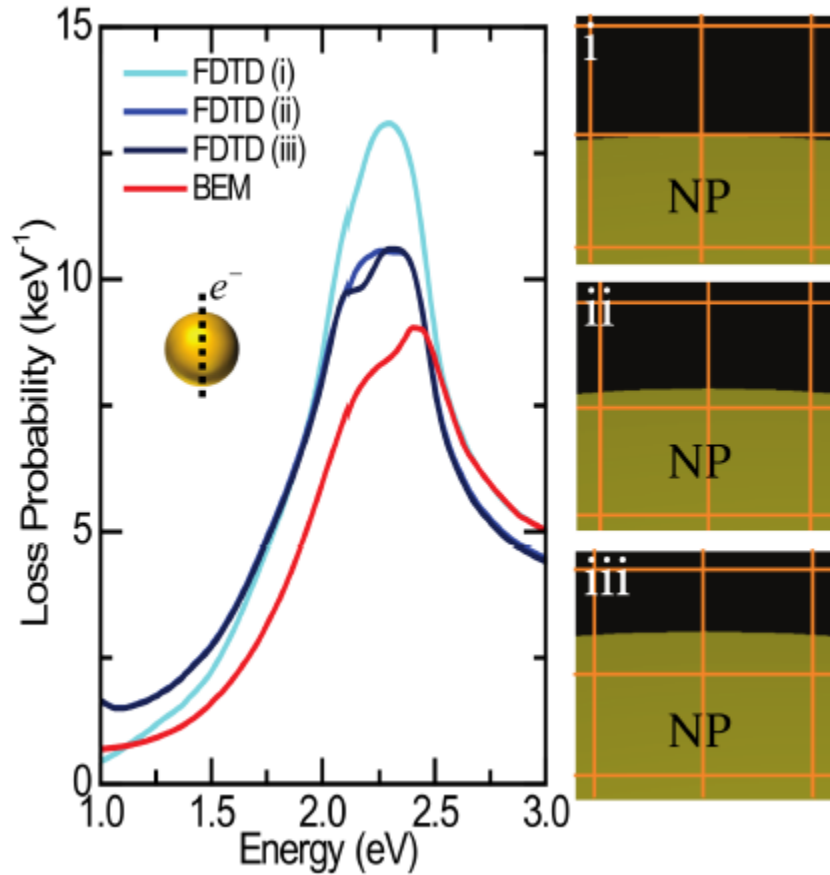
Figure 2.5 – Numerical improvement for penetrating case

2.3.2. Strongly coupled system

Many EELS measurements have been performed to research on dimer structures.[8,10,16,26–28] So here we also have great interest to see the simplest coupling

system's plasmonic properties. The dimer system is made of two silver spheres, whose diameters are both 160 nm. Gap distance between those two silver spheres is only 5 nm. Gap to diameter's ratio is only about 0.03, where strongly coupled phenomenon will happen. Besides, the dielectric function of silver sphere is from Palik data.[24] Other parameters' setting is similar to the gold sphere's situation.
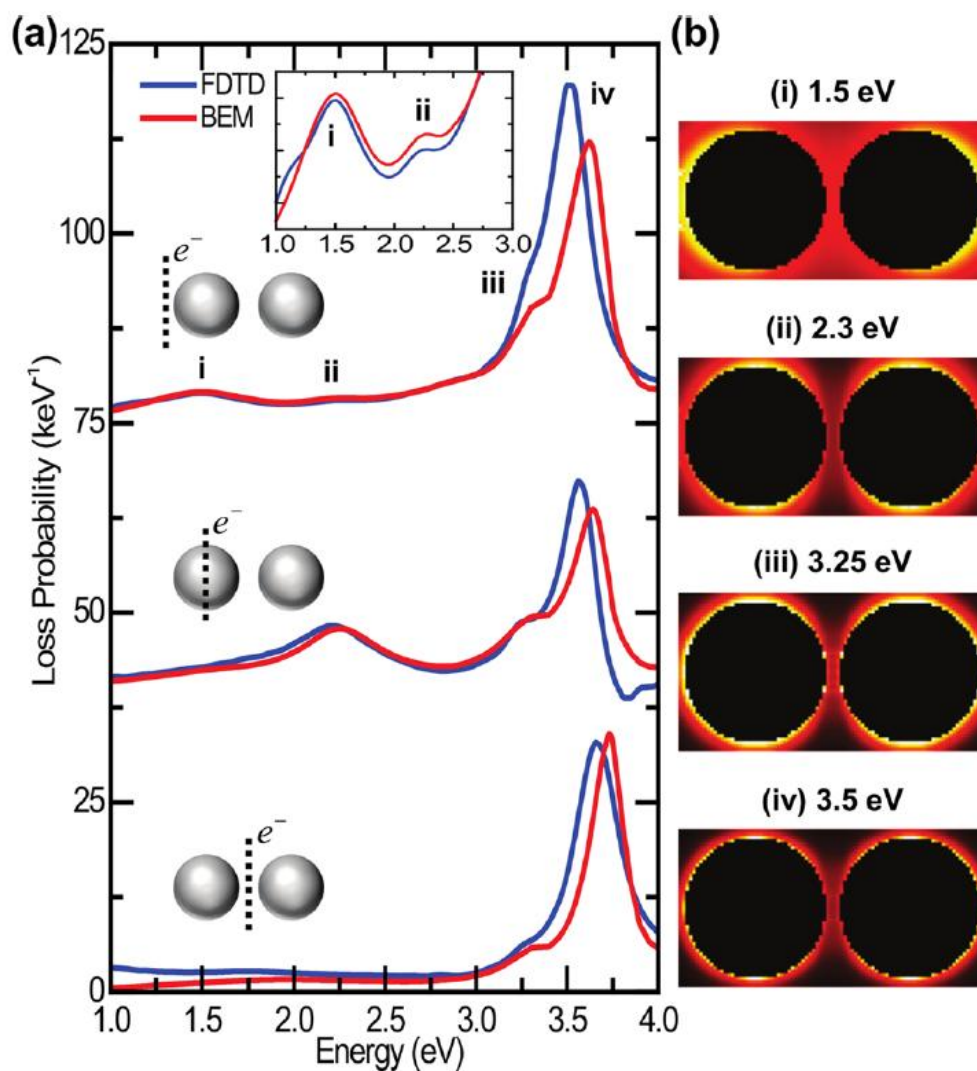
Figure 2.6 – Silver dimer's EELS spectra and maps

Figure 2.6 above shows the EELS spectra for the strong interacting silver dimer. It represents three different cases: (i) Electron beam is near one of the silver spheres, i.e. impact parameter is 164.5 nm. (ii) Electron beam is penetrating one of the spheres, i.e. impact parameter is 82.5 nm (iii) Electron beam is at the center of the gap, i.e. impact parameter is 0 nm. Again, electron's velocity is half of the speed of light. As we know, if the dimer's gap is large enough, it has already been shown the clear bonding and antibonding dipole mode, respectively.[29] However, in our case, gap is extremely narrow compared with their sizes, meaning dimer system is strongly coupled. So based on plasmon hybridization theory (PH),[30] dipole mode will couple with other high order modes such as quadrupole mode, octupole mode etc. There are two low energy modes appearing at 1.5 eV and 2.3 eV, respectively. They are called localized surface plasmon resonances (LSPRs). According to mode analysis of the EELS maps on figure 2.6(b) as well as dark modes excitation by COMSOL, we identified the mode at 1.5 eV to be the longitudinal bonding dipole mode. Meantime, another mode at 2.3 eV was proven to be the transverse bonding dipole mode. On the other hand, we could also see very strong peak intensities at 3.5 eV and a very obvious shoulder at 3.25 eV. Based on the EELS map, peak at 3.5 eV is the antibonding dipole mode while shoulder at 3.25 eV is a strong hybridized mode. For EELS map, we didn't calculate the penetration case for the simplicity. What's more, we applied 4 nm as the spatial resolution for all the maps. Also figure 2.6 shows an excellent agreement between FDTD and BEM. Our results agree with previous research work.[8,16,27,28] Due to the strong coupling effects, bonding dipole mode and antibonding dipole mode has a huge energy gap, approximate 1.5 eV.[27–29]

Besides, transverse bonding dipole mode becomes much more stronger when electron beam penetrates one of the spheres. However, if electron beam goes through gap center of the dimer, transverse bonding dipole mode will almost disappear.[8] So impact parameter plays an important role to determine different modes energy distribution. Finally, since silver particle's size is very large, strong retardation effect will happen. Same mode's peak position will change a little bit when using different impact parameter for electron beam.

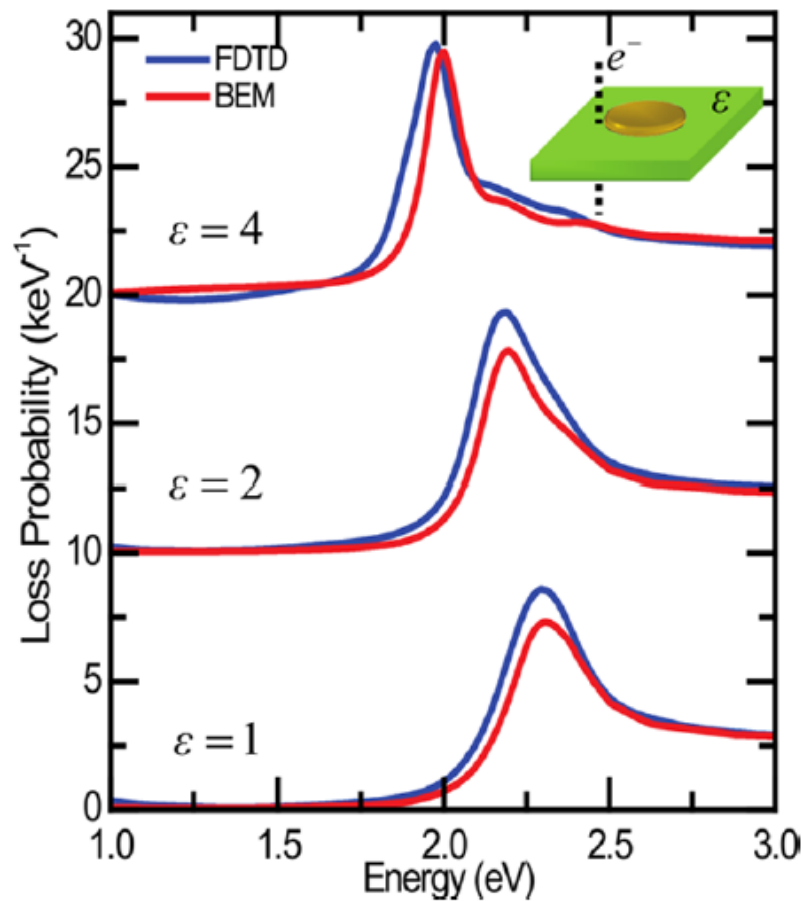### 2.3.3. System with supported substrate

Figure 2.7 – Gold disk on substrate, EELS spectra

In almost every EELS experiment, we found the thickness of substrate was very thin. What's more, non-dispersive material has often been chosen. We did this in order to minimize the energy loss caused by supported substrates. For example, the frequent materials we use are silicon nitride, silica, sapphire etc. Their typical thickness is about 20~40 nm. In previous EELS calculation, most researchers will neglect thin substrate's effect for the simplicity. Here, we found that substrate had a big effect on the EELS spectra as previous paper shown in optical spectra.[31]

In figure 2.7, the gold disk's diameter is 50 nm. The height of it is 15 nm. It has been put on the substrate, whose thickness is 30 nm. Electron beam's impact parameter has been fixed to be 27 nm. So electron is only 2 nm away from the edge of gold disk. Again, electron beam's velocity is half of light in vacuum. For gold disk, we still applied Johnson and Christy experimental data[23] in our interested wavelength region. Different dielectric constants corresponding to different frequent materials have been used for substrates. As can be seen from figure 2.7, dielectric constant is equal to 1 on the bottom, meaning the disk is placed just in vacuum. In the middle, dielectric constant is 2, corresponding to silica substrate. On the top, dielectric constant is 4, standing for silicon nitride.[32,33] Similar to previous system, EELS spectra shows an excellent agreement between FDTD and BEM. Since we have isolated gold disk on the substrate, only LSPR dipole mode appears on the spectra. Besides, peak position is at about 2.3 eV if there is no substrate. Nevertheless, peak position will red shift to approximate 2.0 eV when placing on silicon nitride. This is reasonable due to the change of background medium's effective dielectric function. Another noticeable change is the spectra's line shape. So we could conclude that

substrate matters a lot when we perform EELS simulation and should be included in the accurate calculation.
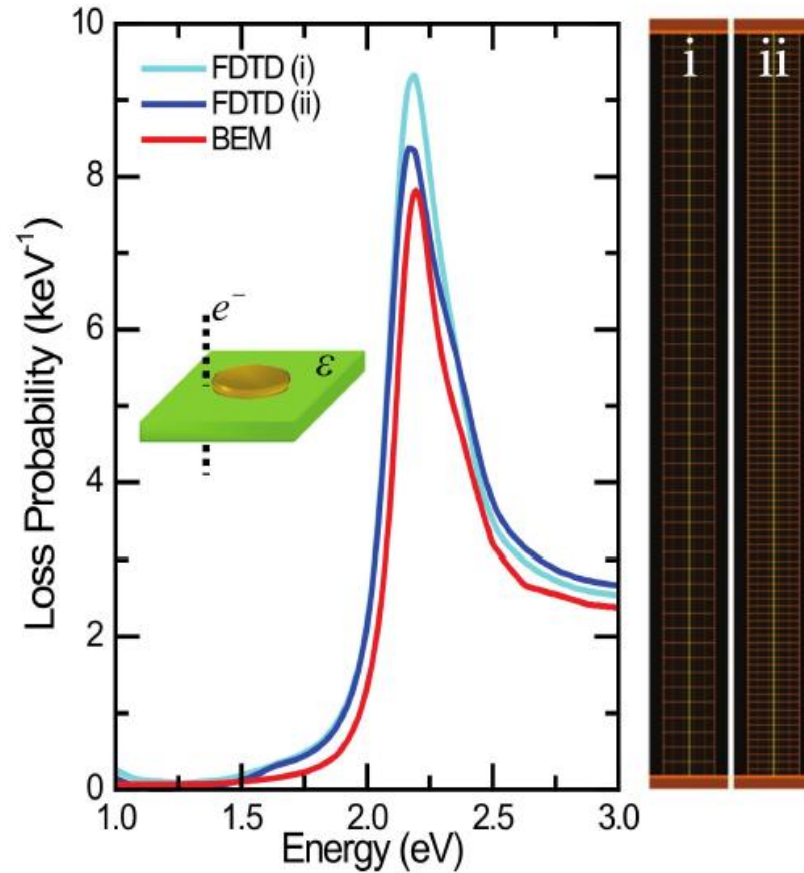
Figure 2.8 – Override mesh effect on EELS spectra

We could further improve our FDTD calculation's accuracy by reducing mesh grid size along electron's moving trajectory as shown in figure 2.8. Case (i) corresponds to 2 nm mesh grid size while case (ii) corresponds to 1 nm mesh grid size. It is shown that the spectra of case (ii) are more close to BEM calculation.

Now let's consider another more complicated geometry: bowtie antenna on silicon nitride substrate. The detailed dimensions are as following: it is made of two equilateral triangles. Each triangle edge length is 80 nm. And each of triangle's height is 15 nm. Gap between two triangles are only 5 nm. So this is also a strong coupling system. Bowtie antenna is made of gold. Substrate is SiN with a thickness of 50 nm. Dielectric constant of SiN is 5.5.[34] Meanwhile, between substrates and bowtie, there is a thin adhesion layer of Cr,[24] whose thickness is 2.5 nm.

Figure 2.9 – Bowtie antenna's EELS spectra and maps

According to figure 2.9, basically we have two different excitation locations. One is edge excitation and the other is gap excitation. Figure 2.9 (a) shows edge excitation

case, which means electron beam is near the edge of one of the triangles. The black, red, purple and blue curve represents electron beam is 15 nm, 10 nm, 5 nm and 2 nm away from triangle's edge, respectively. Figure 2.9 (b) shows gap excitation, meaning electron beam is near the gap of bowtie antenna. The black, brown, red, purpl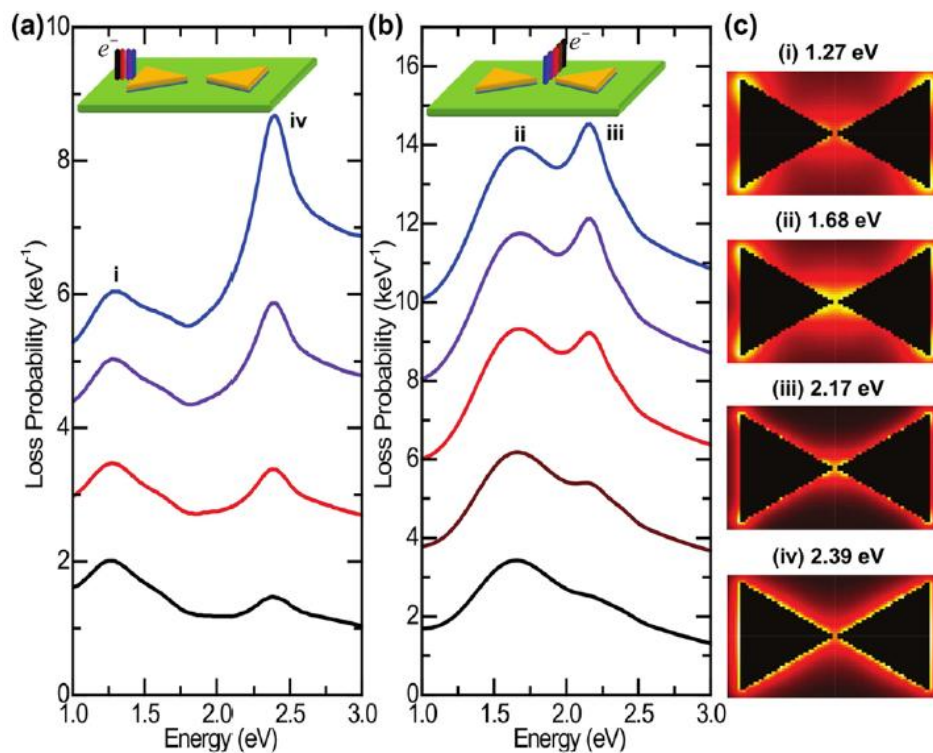e and blue curve stands for electron beam is 15 nm, 10 nm, 5 nm, 2 nm, 0 nm away from the center of gap. For edge excitation, we could see clearly two LSPR modes at 1.27 eV (i) and 2.39 eV (iv), respectively. As impact parameter increases, intensity of mode (i) will keep almost the same while that of mode (iv) will significantly decrease. For gap excitation, again two LSPR modes appear at 1.68 eV (ii) and 2.17 eV (iii), respectively. As electron is much far away from the gap center, intensity of mode (ii) remains the same while that of mode (iii) drops tremendously. Nevertheless, in all of the modes above, peak positions remain the same when changing slightly the impact parameter. These simulation results agree well with previous experimental EELS measurements on the same configuration.[9,35] Figure 2.9 (c) gives EELS maps, whose spatial resolution is 2 nm. In accordance with silver dimer system, we didn't consider the case where electron penetrated the nanostructure for simplicity. From the maps, we could identify each of those four LSPRs modes. Mode (i) at 1.27 eV is bonding dipole mode while mode (ii) at 1.68 eV is antibonding dipole mode. In mode (iv) at 2.39 eV, we can see strong EELS intensity at almost every edge of the bowtie. Hence, it could be regarded as high order mode. For mode (iii) at 2.17 eV, it only shows strong EELS intensity near bowtie's gap. This intensity decreases very fast as impact parameter moves away

from the gap. Figure 2.9 (b)'s peak intensity also verifies our assumption. Those EELS maps agree perfectly with previous experimental EELS measurements.[9,35]
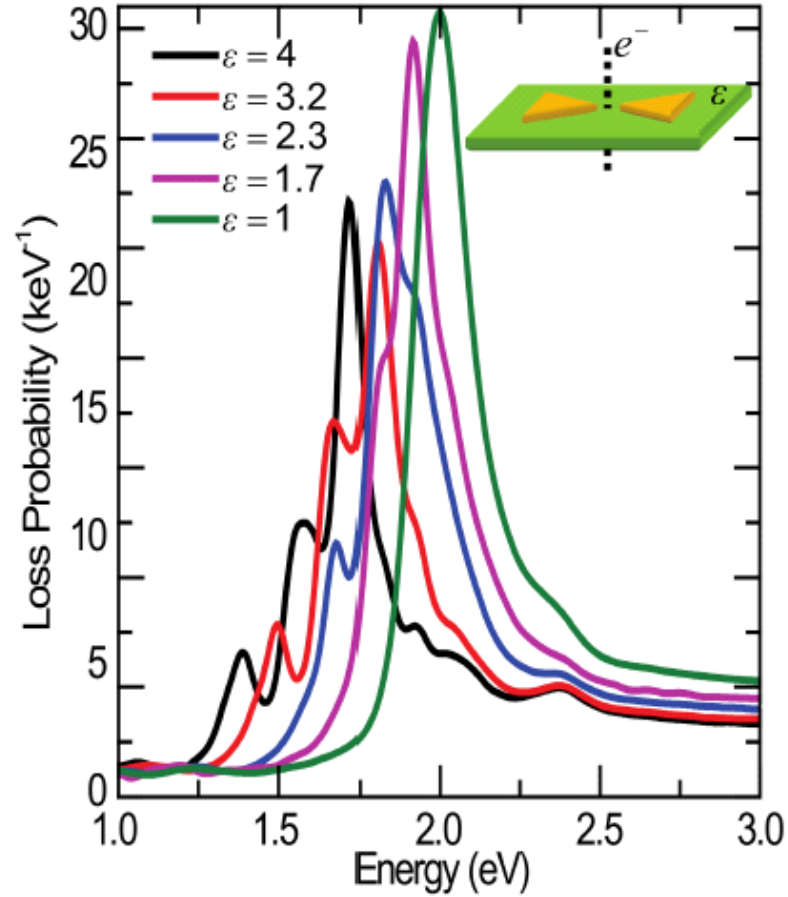
Figure 2.10 – Substrate effects for bowtie antenna

For bowtie antenna, another interesting phenomenon also appears by changing substrate's dielectric constants. As shown in figure 2.10, electron is exactly at the gap center. The bowtie antenna's dimension is the same as previous one. We get rid of adhesion layer for the simplicity. In the simulation, we gradually increase the substrate's dielectric constant from 1, 1.7, 2.3, 3.2 and 4. One similar thing as

previous nanodisk is that LSPR peak will shift to lower energy region. However, unlike previous disk's case, additional high order modes will appear with the increment of substrate's dielectric constant. This tells us bowtie antenna couples much better with substrate compared with isolated nanodisk.
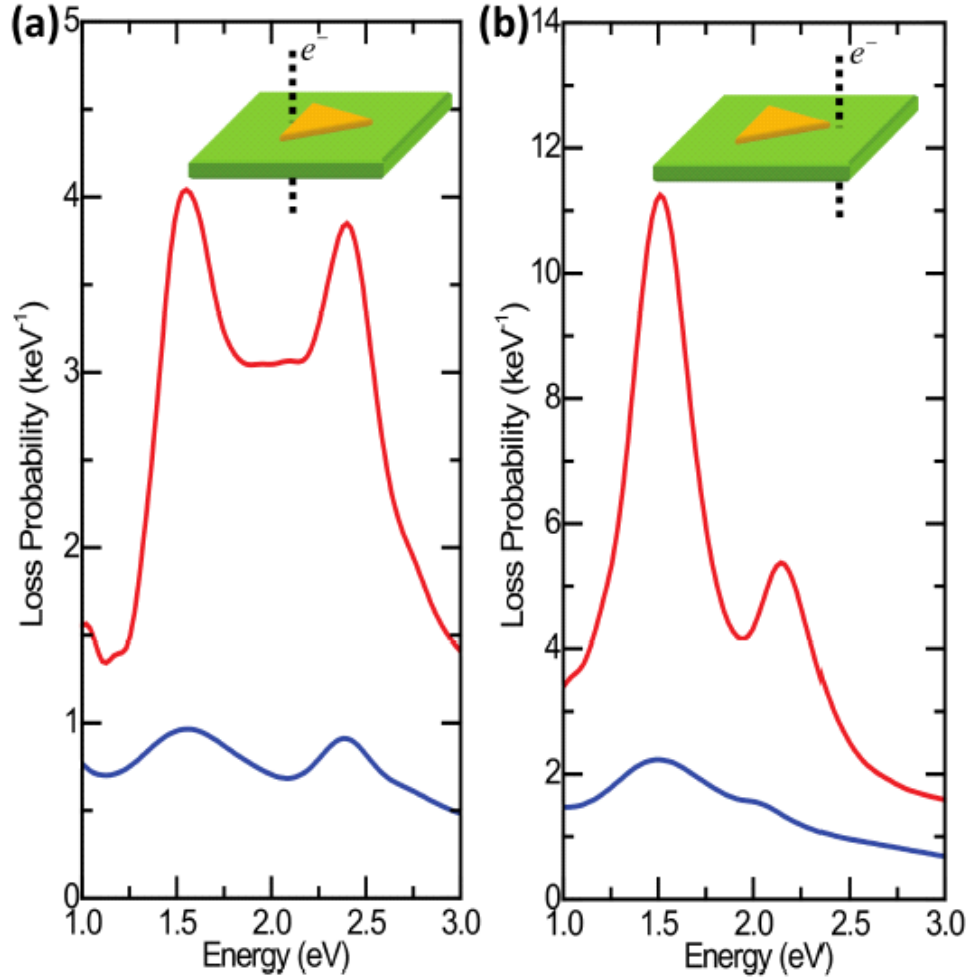
Figure 2.11 – Cr layer's effect for single triangle structure

Besides bowtie antenna, we also simulated single triangle prism's EELS spectra. This time we want to see adhesion layer's effect on the spectra. As shown in figure 2.11,

we also have two different excitation locations: edge excitation and apex excitation. Red lines in both figure 2.11 (a) and (b) represent 1 nm thickness of Cr while blue lines stand for 2.5 nm thickness of Cr. We could find that more Cr layer will make the peak broader. This is reasonable since Cr is a strong absorber and it could be regarded as a damping material. This single triangle prism's EELS-FDTD simulation also shows great agreement with previous work.[9,35]

2.3.4. A real application: high density 2D plasmonic dimers
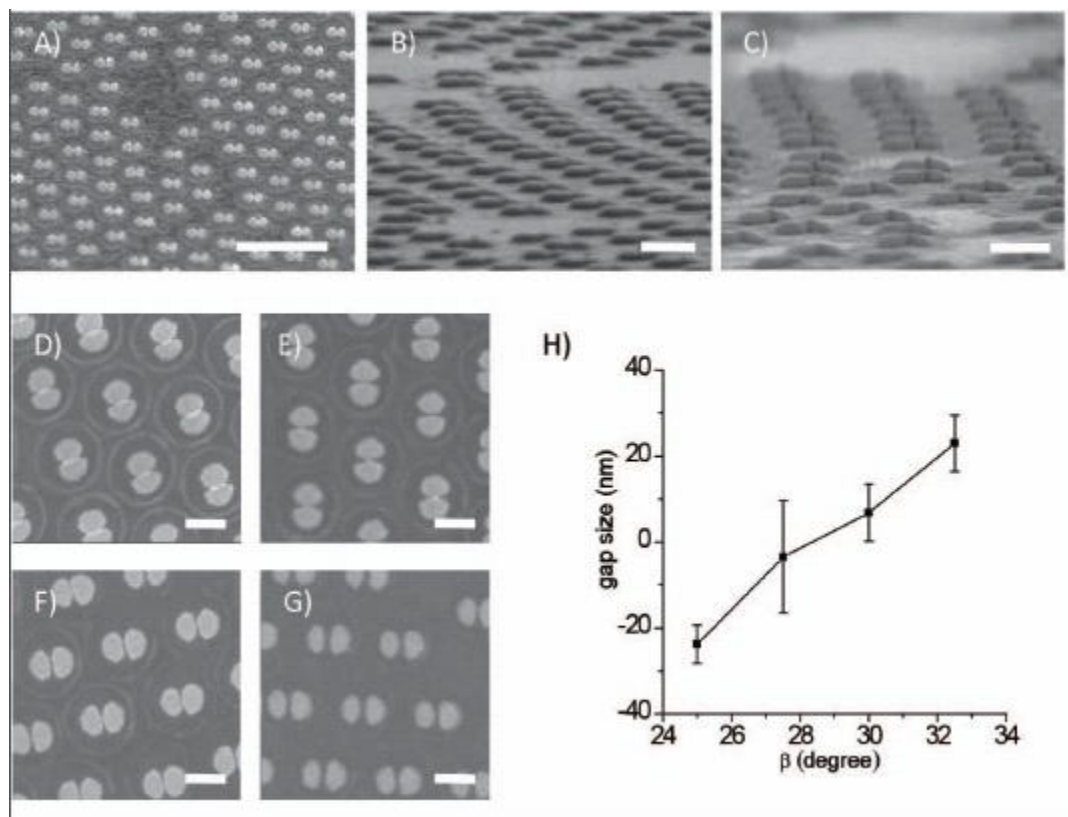
Figure 2.12 – SEM image of Ag-Ag dimer array

Dr. Zhang et al. from Stanford used a brand new technique called nanoimprint lithography (NIL) to fabricate high density Ag-Ag, Au-Au dimer arrays in a very large scale.[36] The gaps between those dimers could be smaller than 10 nm. Figure 2.12 shows the detailed scanning electron microscopy (SEM) image of Ag-Ag dimer array. They had used a myriad of experimental techniques such as scanning electron microscopy (SEM), scanning transmission electron microscopy (STEM), atomic force microscopy (AFM) as well as electron energy loss spectroscopy (EELS) to discover those dimers' plasmonic properties.
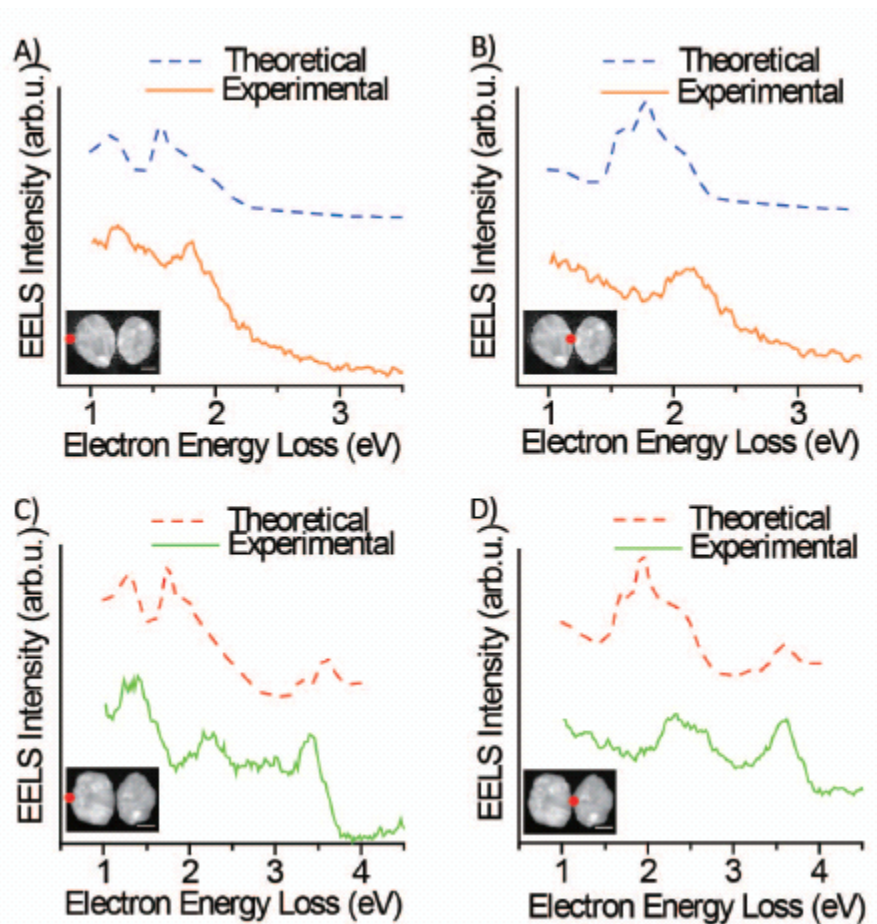
Figure 2.13 – Comparison between experimental and theoretical results

Figure 2.13 (A-B) shows the comparison between experimental and theoretical EELS spectra of Au-Au dimer. One is edge excitation while the other is gap excitation. Figures inset are high-angle annular dark-field (HAADF) images and red spots represent electron beam's impact parameters. We built the model according to HAADF image and applied previous FDTD method[18] to calculate EELS spectra for this specific geometry. Both Au-Au and Ag-Ag dimer could be treated as two hemi-ellipsoids. For Au-Au dimer, the larger ellipsoid's long axis is 190 nm and short axis is 150 nm while the smaller one's long axis is 170 nm and short axis is 130 nm. For Ag-Ag dimer, the larger ellipsoid's long axis is 160 nm and short axis is 130 nm while the smaller one's long axis is 155 nm and short axis is 110 nm. Height is 40 nm and gap is just 5 nm for all of them in the simulation. Johnson and Christy experimental data[23] has been used for gold while Palik data[24] has been applied for silver. Besides, those dimer arrays are supported by silicon nitride substrate[32] with a thickness of 100 nm. From figure 2.13, we found excellent agreement between experimental and theoretical results for both Au-Au and Ag-Ag dimer systems. Since each dimer is well separated, coupling effects between them can be negligible and we only model a single dimer system on substrates. For Au-Au dimer, edge excitation has two LSPR peaks at about 1.2 eV and 1.6 eV while gap excitation has a few LSPR peaks between 1.6 eV and 2.1 eV. For Ag-Ag dimer, edge excitation has three LSPR peaks at about 1.3 eV, 1.9 eV and 3.6 eV while gap excitation has several peaks at 1.8-2.2 eV and 3.6 eV. Here, many different modes have been discovered both in experiment and theory due to the following two reasons: first, gap is so small compared with diameter, meaning two hemi-ellipsoids have been strongly

coupled; second, two hemi-ellipsoids' dimensions are quite different which will also introduce additional modes. Plasmon hybridization (PH) theory could be used to explain for this complicated system.[29,30,36] Interested readers could look through the relevant reference papers.

2.4. Conclusion

A novel EELS calculation based on finite-difference time-domain method has been developed. Details about its principle and implementation have been discussed. This method has shown good agreement with BEM calculation for single gold sphere, silver dimer and disk on substrate. It also gives us great agreement with experimental results for bowtie antenna and semi-ellipsoid dimers on substrate.[18,36] This method is quite robust for solving the following difficult situations: (i) Electron beam penetrates nanostructures (ii) System doesn't have symmetry (iii) Nanostructure has been supported by substrates. Finally, calculating EELS maps by this method could give us a better understanding of different plasmon modes' nature.

Chapter 3

Optical Properties of Split-Ring Resonators (SRRs)

3.1. Introduction

Split-ring resonators (SRRs) could be regarded as one member of the metamaterials' family. Compared with natural materials, metamaterials could show more interesting and surprising properties. Usually, metamaterials could be fabricated in a very large scale. Each unit's dimension among those quasi periodic arrays will be less than the incident light's wavelength. Those structure's geometry and shape will have a big effect on their optical and electric properties.[37] Researching on those metamaterials will show us some novel and interesting phenomena such as negative refraction[38] and Fano resonances[39]. So metamaterials have a wide application in the

following areas: (i) data storage (ii) communication (iii) light harvesting.[40] Like many other 2D shape plasmonic nanostructures e.g. square, rectangle, circular, triangle and hexagon, split ring shape is also a very promising geometry. John Pendry first found SRRs' negative refractive indices (NRI).[41] Other researchers verified this surprising phenomenon experimentally later.[38]

To fabricate SRRs in a large scale is very difficult because optical region of metamaterials is in visible or infrared region. There are several traditional fabrication techniques could be used. They are electron beam lithography (EBL) and focused ion beam (FIB). However, these methods could only fabricate samples in a very small scale, approximate $100 \times 100 \, \mu m^2$. Meantime, these two techniques require very high cost. On the other hand, laser microlens array lithography and laser interference lithography could be used to fabricate in a very large scale.[42,43] Nevertheless, these two techniques require very high and strict optical conditions. Herein, much effort has been put to develop a convenient and easy method to fabricate those metamaterials in large scale. A lot of new methods appear: (i) nanoimprinting lithography[44] (ii) colloidal lithography[45–49] (iii) capillary force lithography[50] etc. Here, a brand new fabrication technique named stretchable colloidal lithography (SCL) has been developed based on colloidal lithography.[51] This method will enable us to generate large scalable SRRs structures at very low cost.

3.2. Fabrication of SRRs
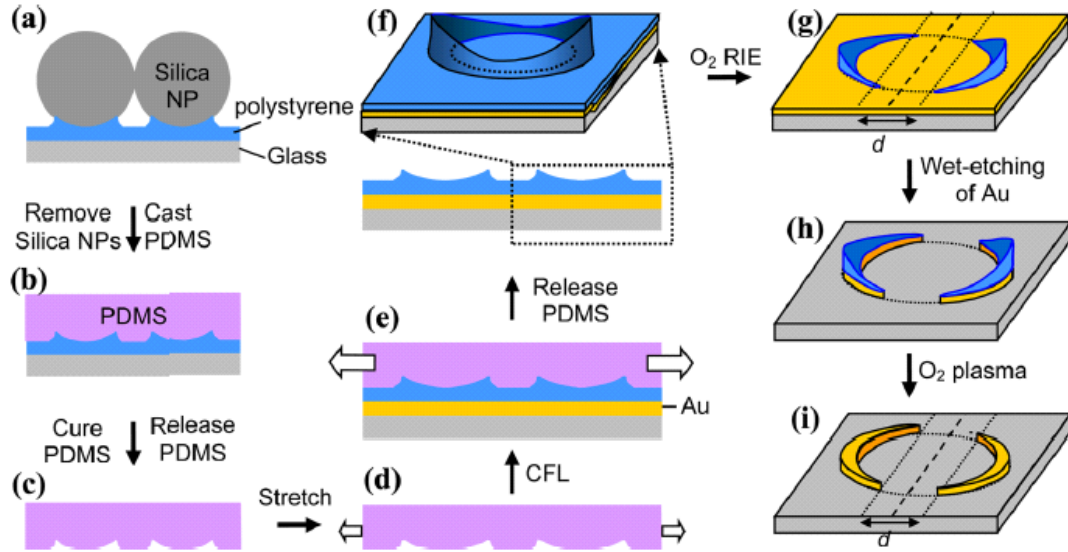
Figure 3.1 – Gold SRRs fabrication's procedure

Figure 3.1 schematically shows the detailed steps to fabricate SRRs via SCL. Previous work has shown to fabricate elliptical rings (ERs) using the same technique.[52] A glass slide has been pretreated by O_2 plasma. The polystyrene (PS) film has then been put onto the glass substrate. After that, many silica nanoparticles have been placed onto PS film. The reason we want to pretreat glass is to make PS film hydrophilic. In order to get circular PS nanorings, we annealed the samples above at 130°C under very dry environment for 10 minutes (Shown in figure 3.1(a)). By using sonic wave technique, we could get rid of silica nanoparticles. Then we cast poly(dimethylsiloxane) (PDMS) and cure for 6 hours at temperature of 70°C (Shown in figure 3.1(b)). Next step, we could release PDMS from PS and glass slide (Shown in figure 3.1(c)). Moreover, we need to stretch PDMS in one direction in order to

first get ERs (Shown in figure 3.1(d)). Later PS film with gold was covered by PDMS mold. Height of gold is 50 nm with 5 nm thickness of Cr as adhesion layer (Shown in figure 3.1(e)). The whole sample has been annealed for about 10 minutes at 130℃. Then we could remove PDMS mold and elliptical nanorings with a variance of height distribution will be formed (Shown in figure 3.1(f)). By using O_2 RIE, ERs could be separated into two half rings (Shown in figure 3.1(g)). With the wet-etching technique, extra gold film can be got rid of where it is not covered by PS film (Shown in figure 3.1(h)). Finally, desired SRRs could be obtained by O_2 plasma (Shown in figure 3.1(i)). The advantage of this technique is that as long as we could fabricate one set of PDMS mold, we needn't repeatedly fabricate it again. All we need to do is to use the same PDMS mold to form SRRs. In practice, more than 30 times has been used for the same mold. This is important because it will make large scale repeated, uniform SRRs.

One important step during all of the fabrication techniques is to stretch circular PDMS mold. Figure 3.2(a-b) show AFM images of PDMS stamp before and after stretching, respectively. We could clearly see the transformation from circular ones to elliptical ones. Figure 3.2(c-d) show AFM line profiles corresponding to figure 3.2(a-b). From these two figures, rings' length and height can be easily obtained. Originally, circular apertures will have diameter of D_0 and height of h_0. After stretched, elliptical apertures' short axis length is D_s with a height of h_s while its long axis length is D_L with a height of h_L.
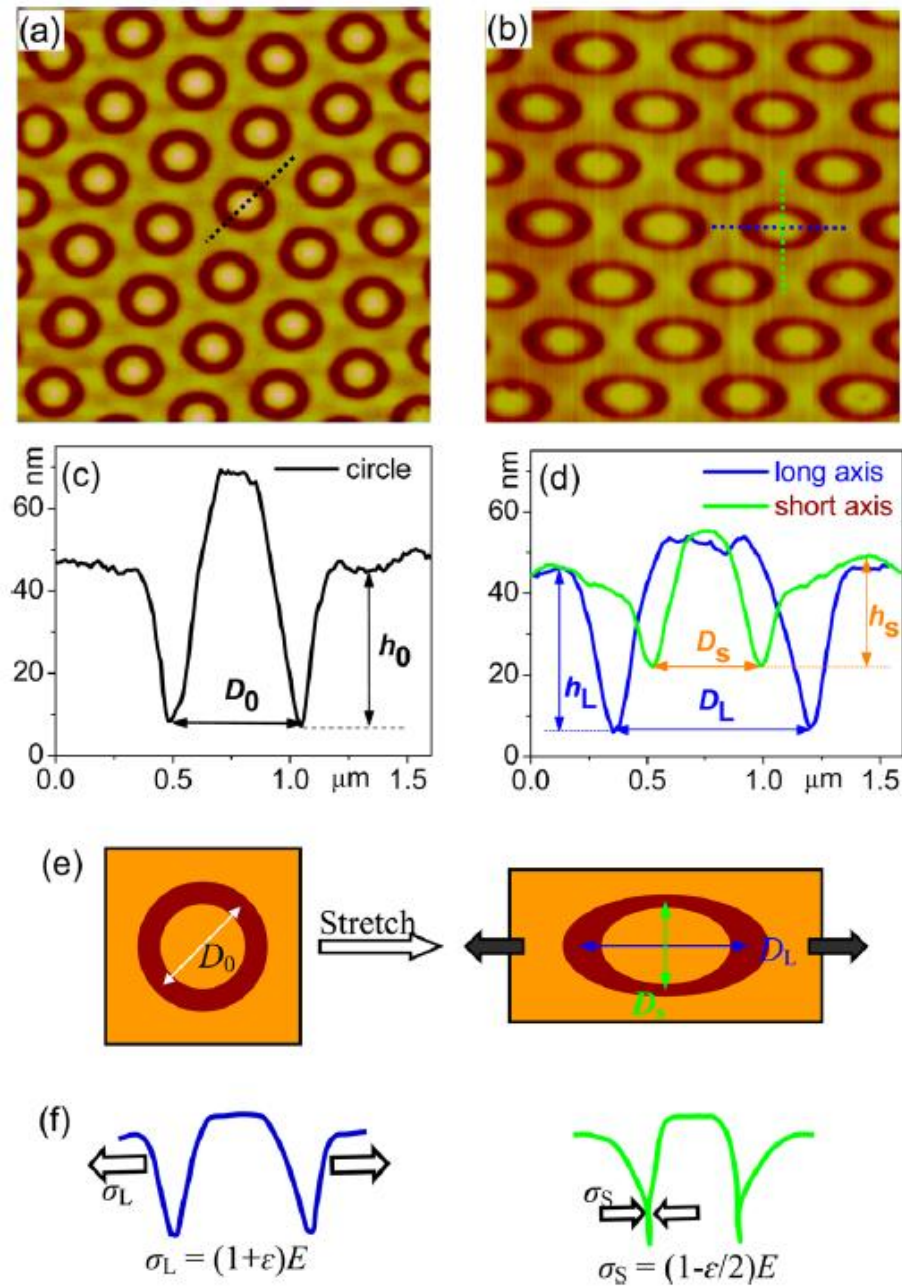
Figure 3.2 – PDMS stretching procedure

The stretching mechanism could be explained by Hooke's law. When we applied an external stress in one certain direction, the length of circular apertures in that direction will be increased while in the vertical direction the length should be

decreased. Meanwhile, height of apertures will also change, especially in the short axis direction as shown in figure 3.2(f). From AFM line profiles, we could further measure those heights quite accurately. We could get h_0, h_L, h_s are roughly 36 nm, 38 nm and 24 nm, respectively. So long axis' height is almost the same as original one's but short axis's height is much smaller than original one's due to Poisson contraction effect.
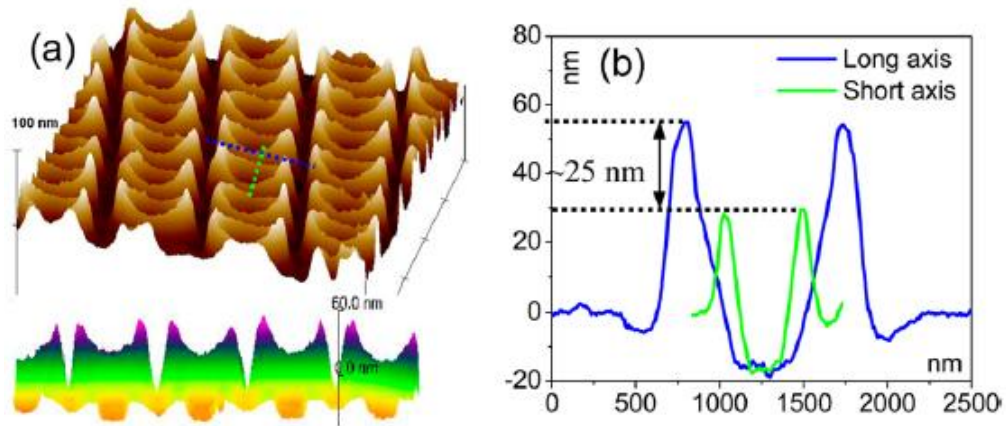
Figure 3.3 – Elliptical Rings (ERs) AFM image
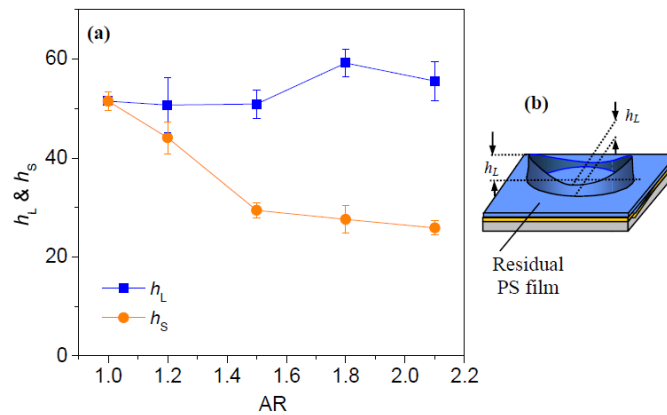
Figure 3.4 – Height for PS film for different AR

After the PDMS stamp has been stretched, we could get elliptical rings as shown in figure 3.3. Again, their heights also have difference. Long axis has the largest height while short axis has the smallest one. Boat shape structure will be formed according to the 3D AFM image view in figure 3.3. Based on AFM line profiles, we could find 25 nm height differences between long and short axis. Here height difference is a very important parameter to consider if we want to fabricate SRRs. If height difference is very small, both long axis and short axis will be etched away during RIE. We define the aspect ratio (AR) as D_L/D_S. As we can see from figure 3.4, long axis' height will be almost the same while short axis' height will drop dramatically before AR arrives at 1.5. If AR is too small (e.g. AR = 1.0 or 1.2), height difference is so small that we couldn't fabricate the appropriate SRRs. Only when AR arrives to 1.5 or larger could it be possible to separate ERs to get SRRs.

Figure 3.5 – SEM images and AFM profles of SRRs

In our experiment, we stretched PDMS mold to elliptical apertures whose AR is equal to 1.8. In this situation, height between long axis and shor axis is 25 nm, large enough to fabricate SRRs. Figure 3.5 (a-b) shows "zoom out" and "zoom in" SRRs array's SEM images on silica substrate, respectively. As shown in figure 3.5(b), gap distance between separated rings is about 260 nm. Since they are well separated from each other, no big coupling effects will happen. So in our later num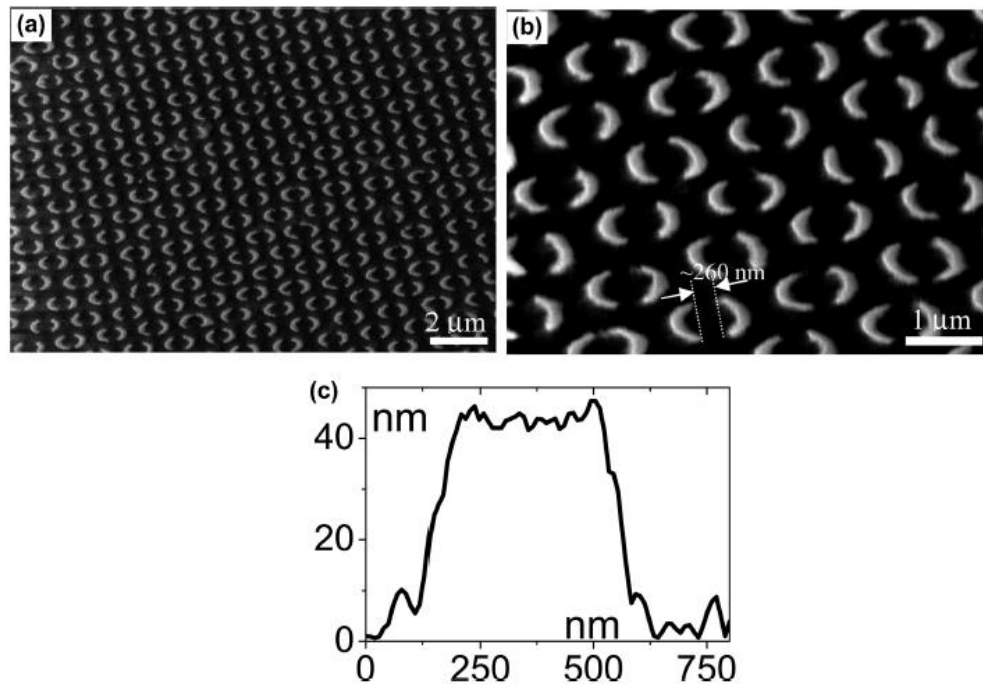erical calculations, building just one pair of SRRs is enough to describe this system instead of more complicated large ensemble of SRRs or periodic array of SRRs. Besides, AFM line profile shows quite uniform height of gold SRRs, about 45 nm.

3.2.1. Control SRRs gap distance

Many different factors will influence SRRs' geometries in each fabrication step, such as size of silica nanoparticles, stretching stress, RIE time and wet etching etc.[52–54] After PS ERs are fabricated, we could still control SRRs gap distance as shown in the following figure 3.6. By changing different RIE time, we could get SRRs with different gap sizes. The longer RIE time is used, the larger gap distance is obtained. The height of polymer ERs is composed of two different parts. ($H(x) = h_0 + h(x)$) Here, h_0 is the thickness of residual PS film on top of gold film. It is a constant, roughly 40 nm. $h(x)$ is the additional height, which will increase step by step from the short axis to the long axis as shown in figure 3.6. Moreover, we could treat $H(x)$ as an even function since the whole structure is symmetric. So the gap distance d can be roughly regarded as two times of x.
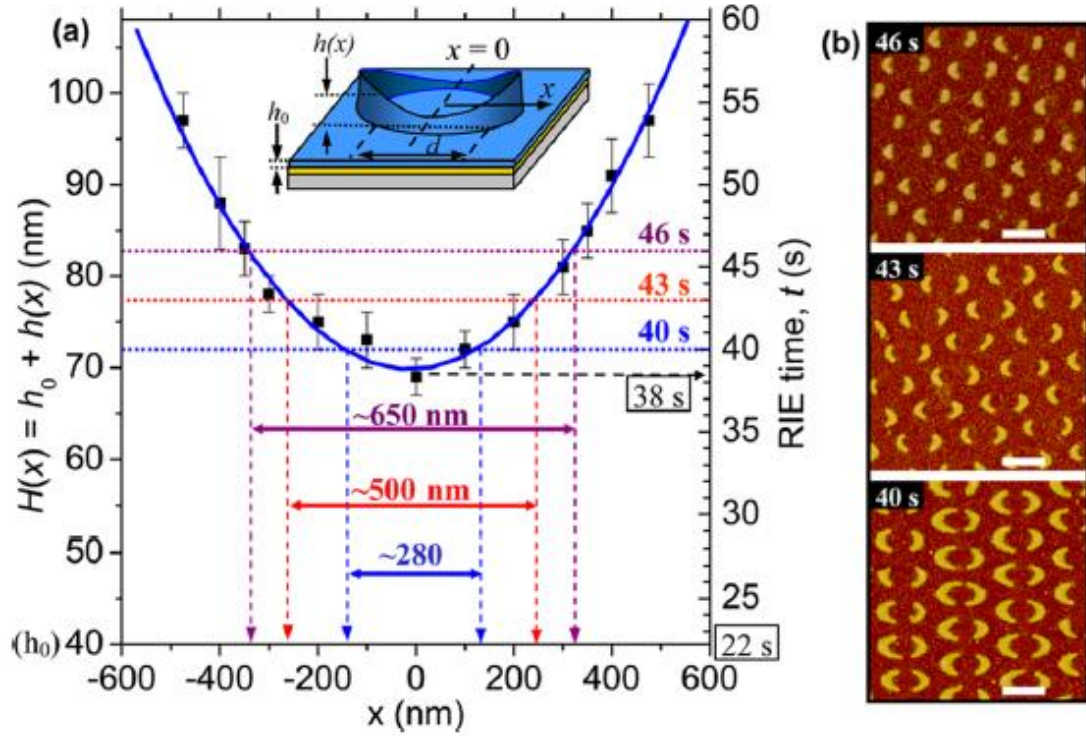
Figure 3.6 – Gap distance of SRRs at different RIE time

According to previous experience,[52] the etching rate for reactive ion etching (RIE) is about 1.8 nm/s. So in order to first get ERs, we need to etch away residual PS film, whose thickness is about 40 nm. This will take us about 22 s based on the etching rate. If we want to further get SRRs, more RIE time is needed. From figure 3.6 (a), we could see closed elliptical rings begin to split at 38 s. When RIE time arrives at 40 s, two split rings are well separated with a gap distance of 280 nm. What's more, gap distance is 500 nm and 650 nm at the time of 43 s and 46 s, respectively. Figure 3.6 (b) also shows the AFM images of SRRs at different RIE time. We could measure the gap distance according to the scale bar in figure 3.6 (b). The measured data are

$260 \pm 55\ nm, 520 \pm 34\ nm\ and\ 627 \pm 36\ nm$ for 40 s, 43 s and 46 s, respectively.

Our predicted values agree perfectly with those experimental ones.

3.3. SRRs' optical spectra and standing wave model
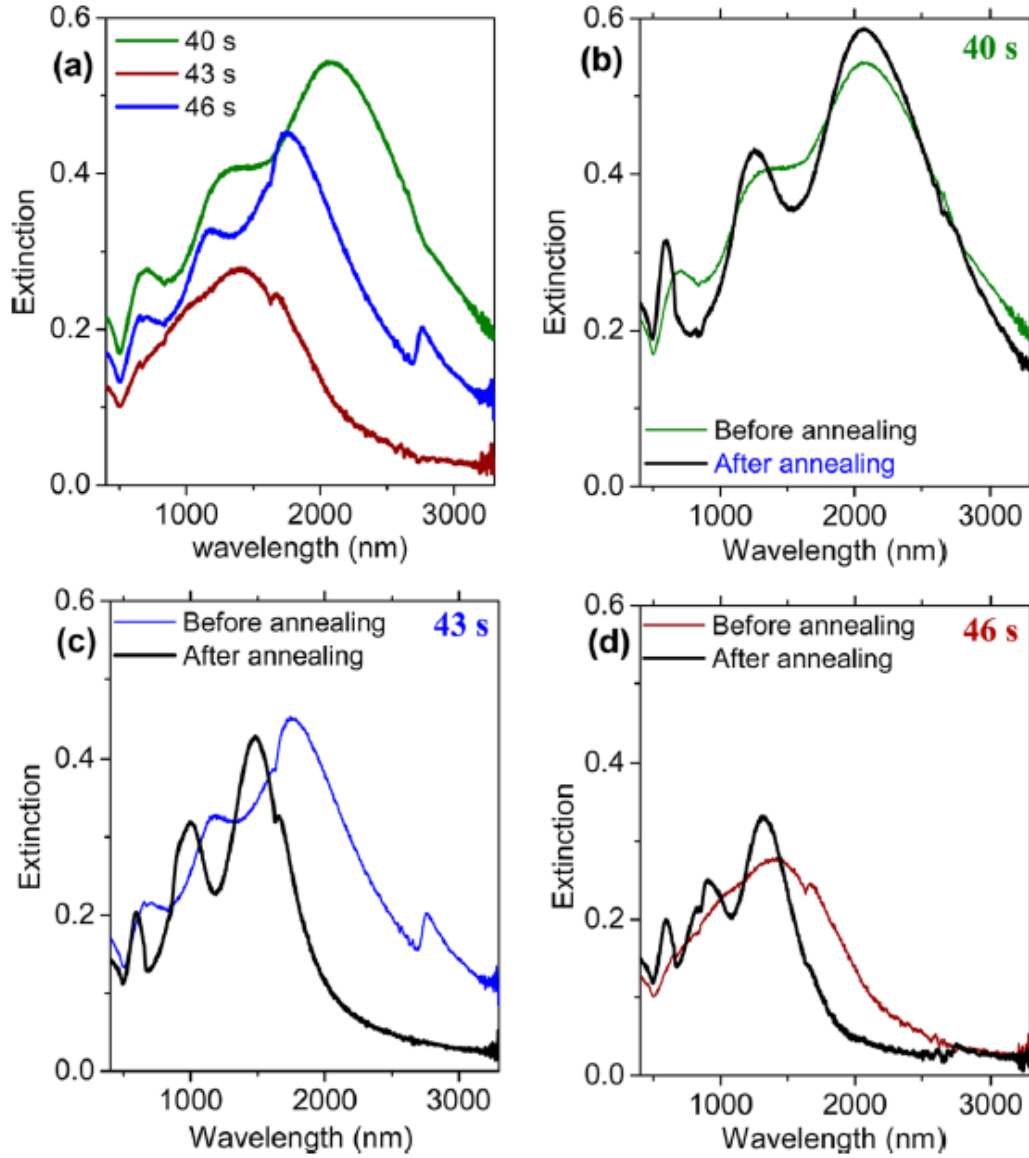
Figure 3.7 – Extinction spectra of SRRs before and after annealing

Once SRRs have been fabricated, UV-vis-NIR equipment has been used to measure its optical properties. Here we applied normal incident angle and wavelength region was from 400 nm to 3300 nm. Figure 3.7(a) shows the extinction spectra of SRRs at different RIE times as previous shown. As RIE time increases, LSPR peaks will be damped and broaden. This is due to the fact that SRRs will become more inhomogeneous and rough at longer RIE time. According to figure 3.7(b-d), we could see LSPR peaks would become more sharp and clear after thermal annealing.[55,56] This is reasonable since annealing will smooth the rough surface. Besides, we can see some of LSPR peaks will shift to high energy region. This is because particles' size will shrink a little bit after thermal annealing.
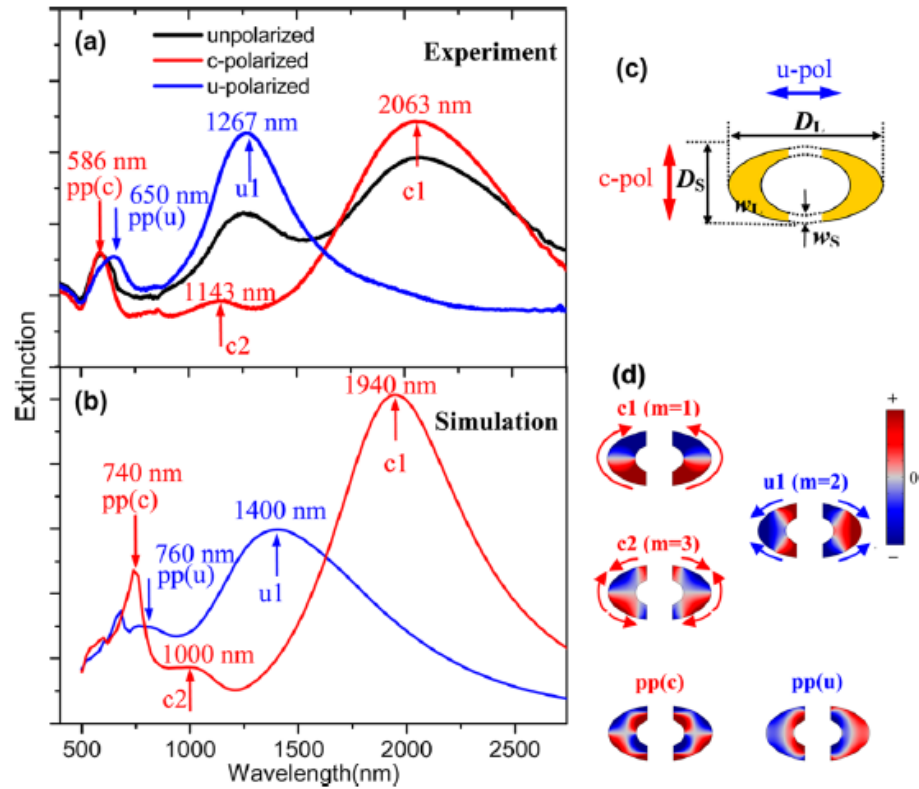
Figure 3.8 – Extinction spectra of Au SRRs both experiment and theory

Figure 3.8(a) shows the experimental extinction spectra at RIE time of 40 s. Both un-polarized and polarized light have been utilized. Regarding the polarized light, two types of polarized lights are used as shown in figure 3.8(c). They are named "c-polarized" and "u-polarized" separately. There are three major resonance modes for c-polarization. Strong dipole mode appears at 2063 nm, named "c1" mode. Another high order and less obvious resonance peak shows at 1143 nm, named "c2" mode. A much high energy peak appears at 586 nm, named "pp(c)" mode. There are only two major resonance peaks for u-polarization. Strong dipole mode appears at 1267 nm, named "u1" mode. Another high energy mode appears at 586 nm, named "pp(u)" mode. Compare un-polarized and polarized spectra, one similarity is major dipole mode peaks "c1" and "u1" will show up. However, less pronounced "c2" mode peak doesn't appear in un-polarized spectra, which is due to its position overlapping with the strong "u1" mode.

We have performed numerical calculations for sake of experimental spectra and nature of each resonance mode. Simulation is using commercial software called "COMSOL", which is based on the finite element method. For SRRs at 40 s of RIE time, the gap distance is 280 nm. Other parameters are used based on SEM images in figure 3.5. D_L is 1118 nm, D_S is 607 nm, w_L is 298 nm and w_S is 140 nm as shown in figure 3.8(c). Johnson and Christy[23] experimental data has been used for gold SRRs. Simulation results are shown in figure 3.8(b). We can see excellent agreement between theoretical and experimental spectra. Slightly different peak positions and intensities are probability due to the following reasons: theoretical models' tips are flat and modeled SRRs' surface is flat while experimental SRRs' tips are rounded and

their surfaces may have some roughness. What's more, inhomogeneous size distribution will happen even if we applied the same PDMS mold to repeat our fabrication.

In figure 3.8(d), charge plots for different resonance modes have also been obtained based on electromagnetic field's Gauss theorem. In those plots, the red color stands for positive charge while the blue color is for negative charge. White area is neutral part, meaning neither positive nor negative charge appears. Arrows in those figures show the induced current's direction according to induced charge's distribution. Each resonance mode could be defined based on standing wave model. Each white strip could be regarded as a node. "c1" mode only has one node in each of SRRs, so m = 1. "c2" mode has three nodes in each of SRRs, so m = 3. "u1" mode has two nodes in each of SRRs, so m = 2. For both "pp(c)" mode and "pp(u)" mode, oscillation and resonance direction is perpendicular to SRRs' tips and contours. Such kinds of special resonances have been observed by previous researchers in small gold nanostructures.[46,48,57]

In previous discussion, we mentioned by controlling RIE time, we could significantly change SRRs' gap distance and geometry. Then extinction spectra had been measured for SRRs at different RIE time as shown in figure 3.9(a). Clearly we can see major peaks "u1" and "c1" will be blue-shift with the increment of gap distance. Besides, "c2" mode only shows at small gap case. When gap distance increases, this mode disappeared. Moreover, pp(c) resonance peak will be a little bit smaller than pp(u)'s.
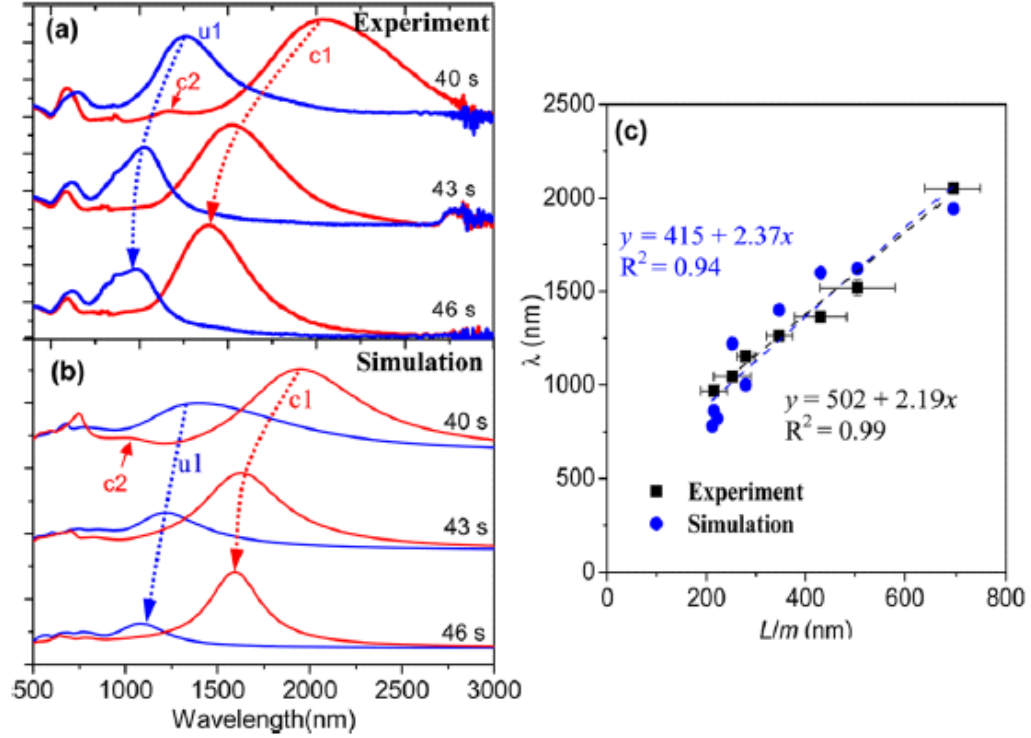
Figure 3.9 – Tunability of SRRs' extinction spectra

Numerical calculations based on FEM have also been performed to get the extinction spectra at different RIE time. We can see simulation results show the exact same trend as experimental results. Major resonance peaks ("c1" and "u1") will blue shift as gap distance increases. Besides, "c2" mode doesn't show up in large RIE time's situation. We could also use standing-wave model to get effective background's refractive index. According to the following formula:

$$L = \frac{m(\lambda + \lambda_0)}{2n_{eff}} \Leftrightarrow \lambda = 2n_{eff}\left(\frac{L}{m}\right) - \lambda_0$$

Equation 3.1 – Standing-wave model

In the equation 3.1 above, m stands for node numbers in each split ring; n_{eff} is the square root of the effective background dielectric function; L is the SRRs' geometric dimension; λ is predicted resonance peak's position; finally, λ_0 is a constant value.[58,59] Equation 3.1 shows the linear relationship between λ and $\frac{L}{m}$, whose slope is just two times the effective background refractive index. So by applying a linear fitting technique for both experimental and numerical results, we could get the approximately effective background refractive index as shown in figure 3.9(c). Experimental data fitting shows effective background refractive index is 1.10 and numerical fitting shows it to be 1.19. Those values agree quite well within numerical accuracy. One of the effective medium theories (EMT) shows the following equation for background refractive index:[60,61]

$$n_{eff} = \sqrt{\frac{n_A^2 + n_S^2}{2}}$$

Equation 3.2 – Effective refractive index

In our case, n_A is the refractive index of air and n_S is the refractive index of silica substrate. Using equation 3.2, we could get the effective refractive index value, which is about 1.26. This value based on EMT will be larger than our previous experimental or simulated results. This is quite reasonable because in EMT, we assume half of the background medium is composed of air while another half is composed of glass. In real case, the percentage of silica substrate will be much smaller than air.

3.4. Conclusion

A novel fabrication technique called stretchable colloidal lithography (SCL) has been developed to produce SRRs in a very large and uniform scale. Furthermore, by controlling stretching stress and RIE time, SRRs' dimensions and gap distances could be changed accordingly. Later we also performed optical extinction spectra measurements and found SRRs' resonance peak ranged from visible to NIR. Numerical calculations based on FEM shown an excellent agreement with experimental results. By using induced charge distribution and standing-wave model, we could better understand the nature of each resonance peak in SRRs. This shows that SRRs have potential application in the biosensor area as one of the most important metamaterials.

<div align="right">Chapter 4</div>

Biomedical Application of Hollow Gold Nanoshells

4.1. Introduction

In our daily life, there are many dangerous diseases strongly affecting our health. Cancer is among one of them. Nanoparticles' technique has been developed recently to deal with cancer.[62–64] Photothermal therapy (PTT) has become an important method to kill tumor cell. Once small nanoparticles have been taken up by experimental bodies, we will shine a light whose wavelength is in the NIR region. This will generate strong plasmon resonance of those nanoparticles. Absorbed light will be transformed into heating, killing those tumor cells. At the meantime, healthy tissue won't have a big absorption effect.[65] In this way, only those "bad" tumor cells

will be eliminated. Many gold nanostructures have shown to be successful in PTT area such as silica-gold nanorods,[66–68] nanocages,[69,70] hollow gold nanoshell[71,72] etc. All of those nanostructures could maintain plasmon resonance peak in NIR region. Many different factors will decide nanoparticles' passive uptake efficiency by tumors, such as particle's size and zeta potential. For instance, it is shown that 45 nm gold particles have better uptake percentage in lung cancer than other large size's gold particle.[73] HGNS core-shell aspect ratio could be highly tunable so that NIR resonance can be achievable by nanoparticle whose size is less than 100 nm.

Many previous researchers have shown HGNS is a very useful material to maintain plasmon resonance peak in NIR region, while total diameters of hollow gold nanoshell could be smaller than 100 nm. They used the following chemical reaction principles: galvanic replacement from high reduction potential to low reduction potential.[74–79] Salt solution usually has high reduction potential while solid metal has low potential. So metal in salt solution will come out but solid metal will dissolve into salt solution. Galvanic replacement formula between gold and silver is as following:[80]

$$3Ag(s) + AuCl_4^-(aq) \rightarrow Au(s) + 3Ag^+(aq) + 4Cl^-(aq)$$
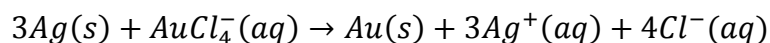
Equation 4.1 – Glavanic replacement between Gold and Silver

Previous researchers have shown the following results: initially we only have solid silver cubes. By reaction formula shown in equation 4.1, gold nanocages whose size is less than 100 nm will be created with resonance peak in the NIR region.[81]

Nevertheless, previous research hasn't paid much attention to those nanoparticles' behaviors inside bodies. Recently, our collaborated group has fabricated HGNS based on silver core with different sizes (e.g. 43 nm, 62 nm and 82 nm). We found its surprising *in vivo* properties.[82]

4.2. Hollow Gold Nanoshells'(HGNS) synthesis
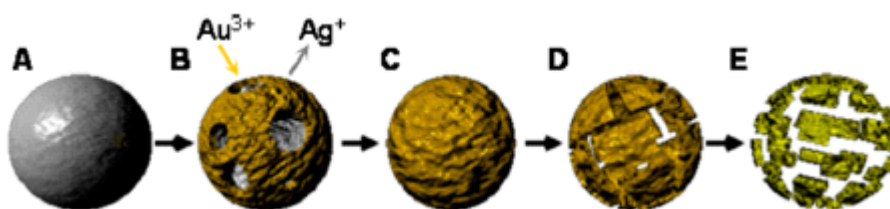
Figure 4.1 – HGNS systhesis procedures

As known from equation 4.1, HGNS could be synthesized based upon galvanic replacement. Figure 4.1 above shows the main five steps of this process. Initially we only have a silver core in the solution (Figure 4.1(a)). Then as chemical reaction begins, silver will go into the salt solution while gold will come out. In this process, pinhole shape geometries are produced (Figure 4.1(b)). Besides, alloy of silver and gold is more stable than any single one component. Due to the Kirkendall effect, silver core will be further dissolved. Later because of Ostwald ripening effect,[80] pinholes on the surface of nanoparticles will gradually reduce (Figure 4.1(c)). However, silver still exists inside the system. Then dealloying stage will again generate a lot of holes around the particles because three silver atoms will go into

solution for just one gold atom comes out according to reaction formula (Figure 4.1(d)). Finally, as all of silver atoms go into solutions, porous hollow gold nanoshells will be formed (Figure 4.1(e)).

4.3. Optical properties of HGNS

Different silver core sizes have been used such as 40 nm, 60 nm and 80 nm. By using the synthesis above, HGNS could be formed. Their dimensions as well as error bars are shown as following : $43.1 \pm 3.9\ nm, 61.8 \pm 3.3\ nm\ and\ 82.6 \pm 4.2\ nm$.
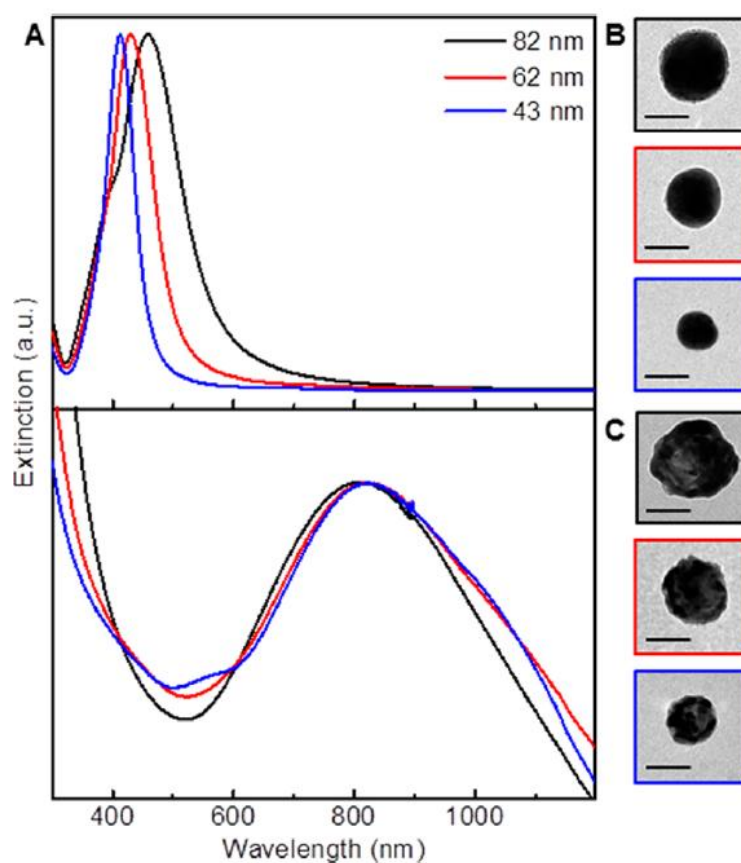
Figure 4.2 – Extinction spectra of colloid Ag and HGNS

Figure 4.2(A) gives experimental extinction spectra of different sizes solid silver and HGNS. Figure 4.2(B-C) shows TEM images of them. We could see clearly that resonance peak is just around 450 nm for colloid silver. However, when HGNS has just been formed, peak position dramatically shifts to about 800 nm, which will be in the NIR region. Meantime, it is shown from figure 4.3 that plasmon resonance peak will blue shift significantly as we increase reaction time up to 24 hours. In order to maintain NIR peak resonance, only a limited reaction time is permitted (e.g. 1 hour time period). X-ray photoelectron spectroscopy (XPS) is a very useful tool to detect different metals' percentage in HGNS. From figure 4.4, we could see at the beginning of the reaction, silver has 80% while gold has only 20%. However, as the reaction continues up to 24 hours, silver and gold have almost 50%, respectively. This tells us silver core plays an important role to maintain peak in NIR.
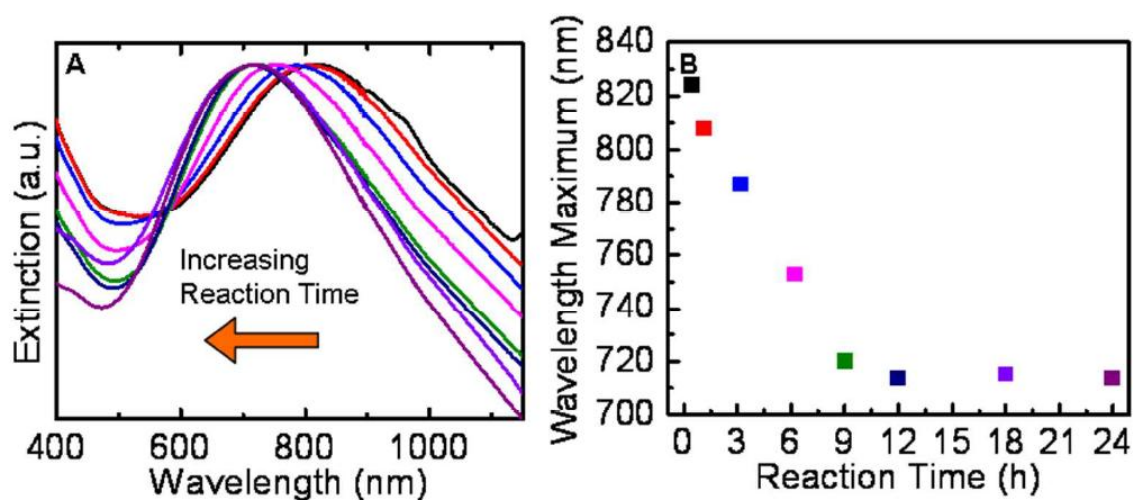
Figure 4.3 – Resonance blue shift as reaction time increases
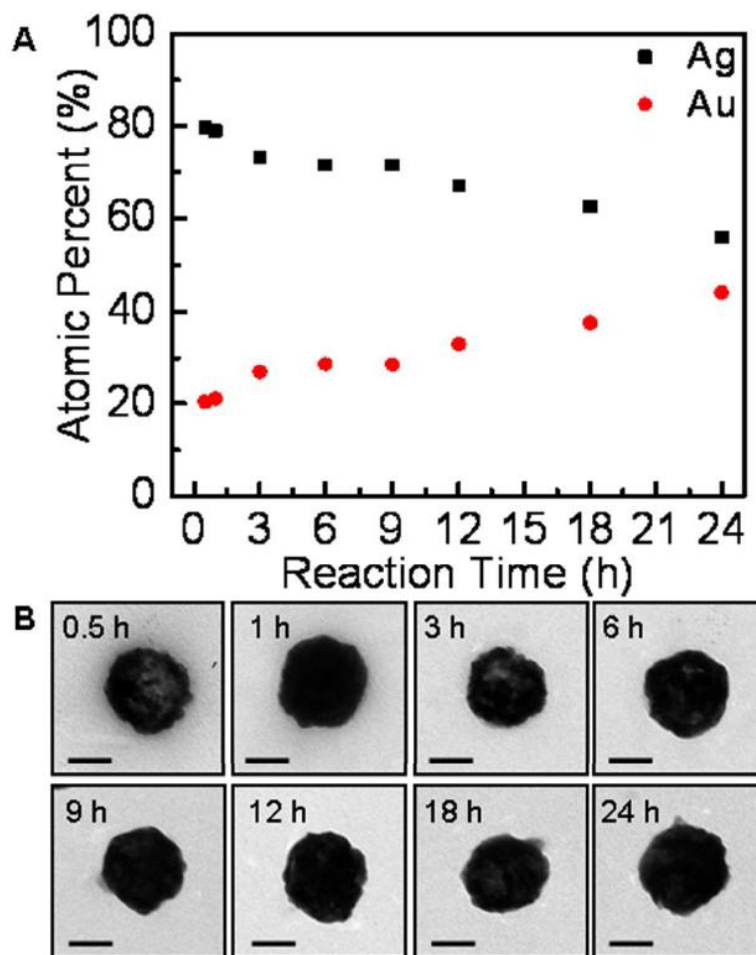
Figure 4.4 – HGNS different metals' percentage and TEM images

4.4. Numerical Modelling of HGNS

In order to better understand experimental peak's significant shifting effects, numerical calculations based on FEM have been performed. From the SEM images shown in figure 4.5(A), HGNS has many defects and holes on its surface. Besides, three silver atoms will go into salt solution for just one gold atom. So nanoparticles will be porous and water could go inside the particle.
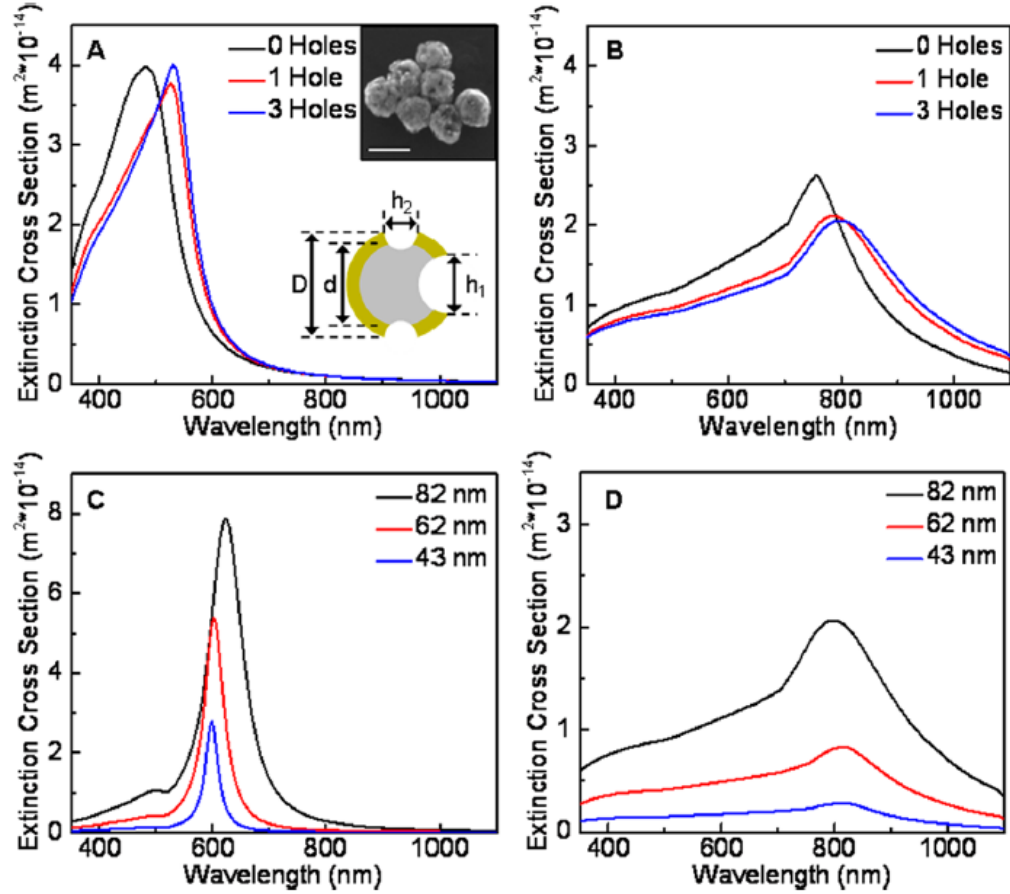
Figure 4.5 – Extinction spectra of HGNS based on FEM

According to experimental conditions, we modeled the shell of HGNS as porous alloy, which is a mixture of gold, silver and water. The core of HGNS was modelled as porous silver, a mixture of silver and water. For the sake of dealing with different dielectric functions' mixture effects, Bruggeman effective medium theory (EMT) has been employed.[83] There are many different types of EMT. The reason that we choose to use Bruggeman EMT is due to its wide application in porous materials.[84] For only two composites, equation shown as below:

$$f_1 \frac{\varepsilon_1 - \varepsilon_{eff}}{\varepsilon_{eff} + g(\varepsilon_1 - \varepsilon_{eff})} + (1 - f_1) \frac{\varepsilon_2 - \varepsilon_{eff}}{\varepsilon_{eff} + g(\varepsilon_2 - \varepsilon_{eff})} = 0$$

Equation 4.2 – Bruggeman EMT for two composites

In our case, ε_1 is silver's dielectric function and ε_2 is water's one. Spherical inclusions are considered so that geometric factor g is equal to 1/3. f_1 is silver's volume fraction. ε_{eff} is the effective dielectric function of the whole system. For porous alloy, it contains three different materials: water, silver and gold. So we need to apply a more generalized Bruggeman effective method:

$$\sum_i f_i \frac{\varepsilon_i - \varepsilon_{eff}}{\varepsilon_{eff} + g(\varepsilon_i - \varepsilon_{eff})} = 0$$

Equation 4.3 – Generalized form of Bruggeman EMT

For porous alloy case, parameter "i" is equal to 3. For high order equation, we always have many different solutions. Since there is no gain medium for the materials we used, solution is chosen so that imaginary part of dielectric function is always positive. For the initial materials, we applied Johnson and Christy experimental data[23] for both gold and silver. For water, real part of dielectric function is 1.77 while imaginary part is 0. By using those data in Bruggeman EMT, we could get desired dielectric function for both porous silver and porous alloy as shown in figure 4.6. For porous alloy, the percentage of water, silver and gold are 46%, 43.2% and 10.8%, respectively. In experiment, we could only determine percentage of silver and gold via XPS but couldn't know the exact percentage of

water in the porous HGNS. So we determined water percentage from simulation to get the expected plasmon resonance at around 800 nm.
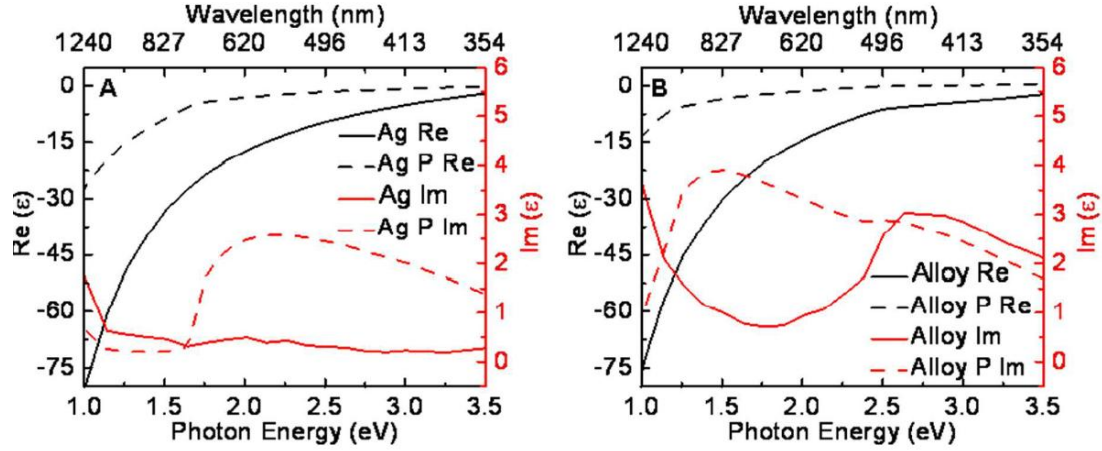
Figure 4.6 – Dielectric function based on Bruggeman EMT

Regarding the specific geometry of HGNS, we have "no hole", "one hole" and "three holes" models, respectively. The "three holes" model is closest to real case since there are many holes around particle's surface. Besides, for "one hole" and "three holes" geometries, particles are not isotropic. When we try to get the extinction spectra, polarization average has been performed. For all the simulations shown in figure 4.5, the background medium is water. As shown in figure 4.5(a), the total diameter of nanoparticle is "D" and shell thickness is "D-d", which means inside silver core's diameter is "d". Besides, for "three holes" case, there are two small holes with a diameter of "h_2" while there is a large hole with a diameter of "h_1". For "one hole" case, there is only one big hole with a diameter of "h_1". Detailed parameters for three different sizes' particle have shown in table 4.1.

Ag Core Size	HGNS Outer Diameter (D)	HGNS Inner Diameter (d)	Large Hole Diameter (h_1)	Small Holes Diameter ($h_2 = h_3$)
80 nm	82.6 nm	66.6 nm	60 nm	30 nm
60 nm	61.8 nm	49.8 nm	45.4 nm	22.8 nm
40 nm	43.1 nm	35.1 nm	31.2 nm	15.6 nm

Table 4.1 – Parameters used in FEM simulations

Figure 4.5(A) shows no porous case, where the percentage of silver and gold are 80% and 20% based on XPS data at the beginning of reaction time. "no hole" case just leads to plasmon resonance peak at about 480 nm. Even for "three holes" case, plasmon resonance peak shifts to around 530nm, which is too far away from the experimental measurement as shown in figure 4.2(A). Besides, we could see "holes effects" just introduce a tiny peak red-shift, which is about 50 nm. Nevertheless, when porosity has been included as shown in figure 4.5(B), we could see a significant resonance peak's red shift, about 275 nm. Comparing figure 4.5(A) and 4.5(B), we can see porosity plays an important role to shift plasmon resonance's peak into NIR region. Again, in this case, "holes effects" only contributes to about 50 nm red shift. In order to verify whether inside core is silver or water, we further perform Mie theory calculation and results are shown in figure 4.5(C). We simulated for different sizes and "no hole" cases. Percentage of silver and gold are 80% and 20%, respectively. Dimensions are exact the same as table 4.1. We could see plasmon resonance peaks are between 600 nm and 640 nm, still far away from

experimental results. This simulation test confirmed us that inside core was really silver.
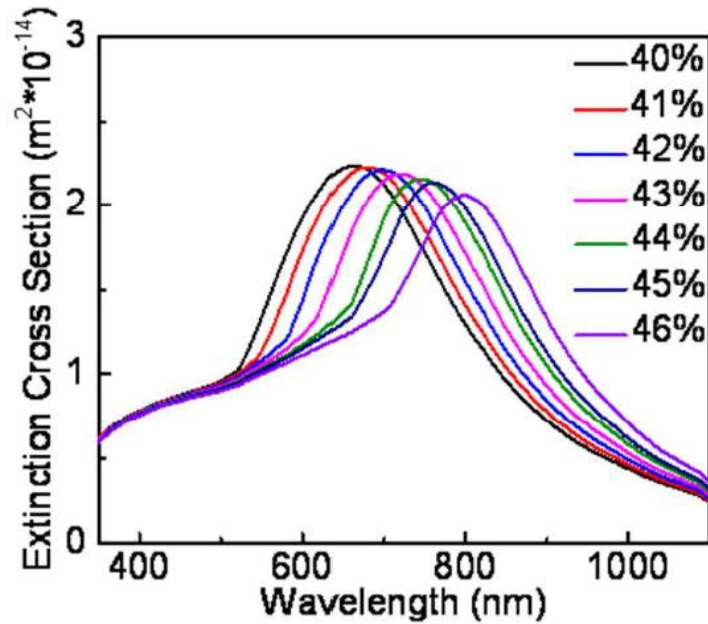
Figure 4.7 – Extinction spectra of different porosity's HGNS

When we compared experimental spectra in figure 4.2(A) and numerical calculation in figure 4.5(D), we found that experimental spectra's resonance peak would be much broader than numerical one's. In order to account for this discrepancy, numerical simulations based on various porosities have been performed and results are shown in figure 4.7. By changing water percentage in HGNS from 40% to 46%, plasmon resonance has a tremendous increase from 660 nm to 810 nm. On the other hand, considering porosity difference is reasonable since each particle among ensemble measurements will have quite different sizes and porosities. After we do an average of simulated extinction spectra as shown in figure 4.7, resonance peak

will be almost as broad as experimental one's. Finally, figure 4.5(D) shows plasmon resonance is about 815 nm for 43 nm HGNS, with porosity of 46.4%; plasmon resonance is around 815 nm for 62 nm HGNS, with porosity of 46.3%; plasmon resonance is approximately 800 nm for 82 nm HGNS, with porosity of 46%.

4.5. Stability of HGNS under laser

HGNS should be coated with polyethyleneglycol(PEG) if we want to test its effect in biological body. There are basically three reasons that we need to do this. Firstly, it will increase HGNS's circulation time *in vivo*.[85,86] Secondly, it will be easier to be swallowed by phagocytes.[85–87] Thirdly, it could make HGNS's surface charge to be almost neutral.[87] There are basically two steps needed to covered by PEG with zeta potential to be -10 mV. First, 10 000 MW thiol-PEG-methyl has been used to coat HGNS; second, 10 000 MW thiol-PEG-amine was added to increase HGNS's density. Table 4.2 below shows extinction spectra and zeta potential for silver colloid, HGNS and HGNS@PEG, respectively.

particle type	80 nm		60 nm		40 nm	
	extinction max (nm)	zeta potential (mV)	extinction max (nm)	zeta potential (mV)	extinction max (nm)	zeta potential (mV)
Ag colloid	458	-49.7 ± 2.2	430	-48.6 ± 1.0	412	-46.9 ± 0.9
HGNS	811	-30.6 ± 0.2	826	-35.2 ± 0.6	825	-41.7 ± 1.0
HGNS@PEG	804	-12.3 ± 0.1	806	-11.1 ± 0.2	787	-9.8 ± 1.6

Table 4.2 – Different sizes particles' extinction and zeta potential
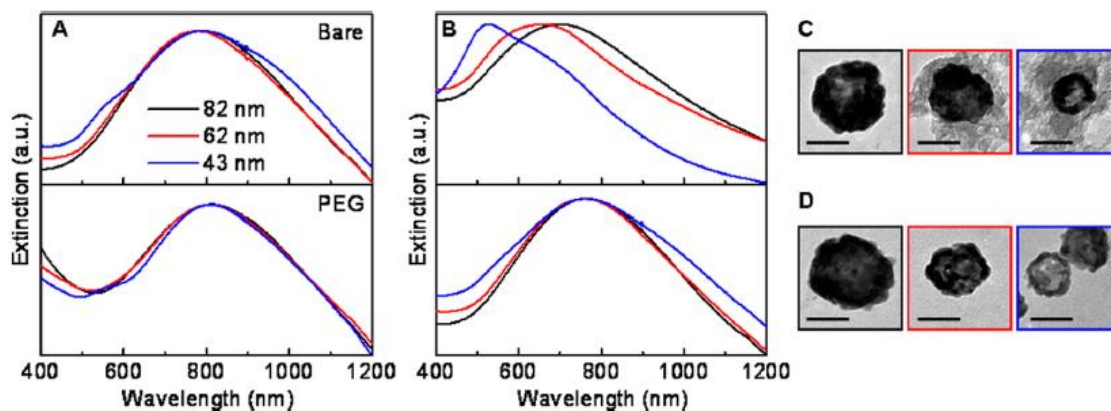
Figure 4.8 – Effects of laser on HGNS and HGNS@PEG

Since HGNS has very large core-shell aspect ratio, thickness of HGNS will be very small. So generated heat can easily diffuse to surrounding medium and kill tumor cells.[77] From figure 4.8, we could see bare HGNS will have different plasmon resonance positions for different sizes' particles with smallest one shifting to bluest side after laser irradiation. However, if HGNS has been pre-processed with PEG, plasmon resonance will almost maintain in the same position for different sizes after laser irradiation. From the TEM images on figure 4.8(C-D), it is easily to see silver leak out for smaller sizes bare HGNS while this phenomenon doesn't happen to HGNS@PEG. So we can conclude that HGNS@PEG will be more stable and appropriate for us to perform *in vivo* experiment.

4.6. Abnormal *in vivo* distribution of HGNS
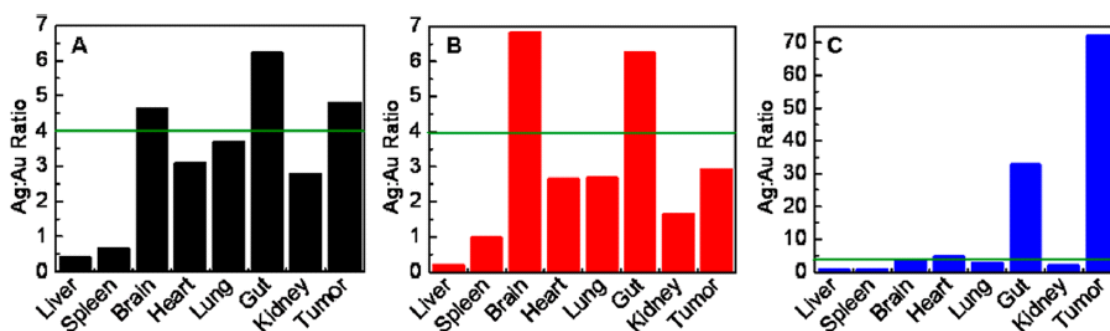
Figure 4.9 – Silver and gold's distribution at different organs

For *in vivo* experiment, we performed it on mice. HGNS@PEG has been used for its stability properties *in vivo* as shown previous. Three different sizes HGNS@PEG (43 nm, 62 nm and 82 nm) have been applied and totally there are nice mice. Any three among the nice mice are set for one group with one specific nanoparticle's size. Later unfortunately, all of them are dead after 24 hours. Figure 4.9 shows Ag/Au ratio in different organs for three different sizes. (A is for 82 nm, B is for 62 nm and C is for 43 nm) They are measured by inductively coupled plasma mass spectrometry (ICP-MS). Green line shows aspect ratio of Ag and Au is 4 before HGNS has been taken in by mice. We could see aspect ratio is quite different at different organs. There is more gold percentage than silver's in liver and spleen. For the aspect ratio in other organs, they are more close to 4:1. However, there still exist some variations either above or below 4:1. Ag/Au aspect ratio is not a constant at different organs indicates that HGNS fragmented sometime after being injected into mice. Besides, we could see variation of Ag/Au aspect ratio is most significant for

the smallest size as seen in Figure 4.9(c). This is reasonable because according to table 4.1, smallest HGNS has the thinnest shell, which means inside silver core is easier to leak outside. As we know, silver is toxic for biological body such as mice.[88,89] So that's the reason why all of the mice were dead within one day.

4.7. Damping effects in hollow gold-cobalt nanoshell

Recently, we have also shown cobalt's tremendous damping effects in HGNS,[90] which has potential in hot electron generation. Figure 4.10(A) below shows Mie theory calculations for hollow gold-cobalt nanoshell with different percentages of cobalt. Johnson and Christy experimental data for both gold and cobalt[23] have been used in the simulation. Again, Bruggeman effective medium theory[83] has been applied to deal with effective dielectric functions of mixed Au and Co. We could see clearly from figure 4.10 that LSPR resonance peak becomes broader and broader as the percentage of cobalt increases. Full width at half maximum (FWHM) has been calculated based on Lorentz fitting of each curve. It is shown FWHM increases almost linearly with the increase of Co percentage in the nanoshell. Experimental measured data in figure 4.10(B) agrees well with our numerical results.
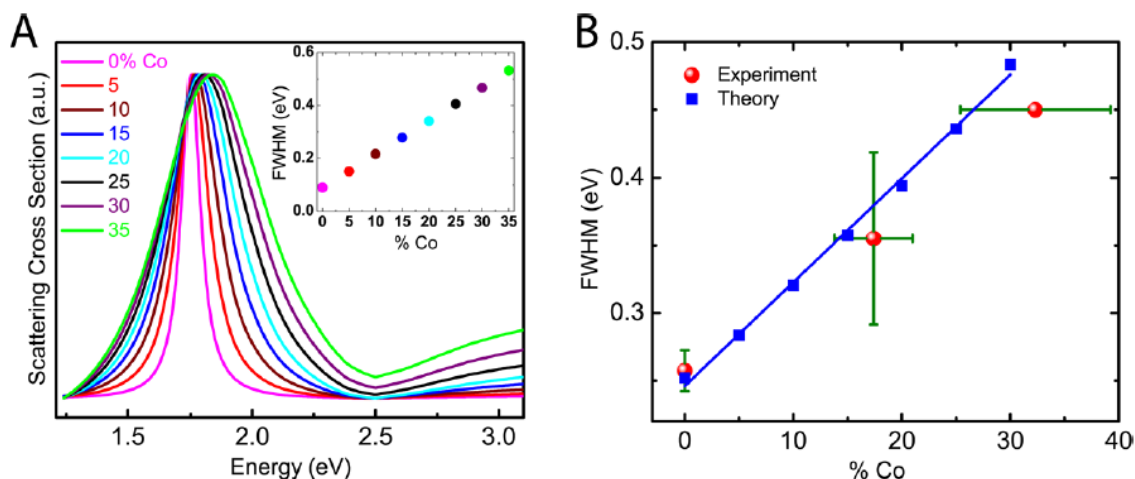
Figure 4.10 – Mie calculation for a variation of cobalt percentage

4.8. Conclusion

We synthesized HGNS nanoparticles with three different sizes ranging from 43 nm to 82 nm. Then ensemble extinction spectra show all different sizes' LSPR peak in the NIR region, which is very useful in biomedical area. Numerical calculations based on FEM were performed. In order to model different materials' mixture effects, Bruggeman effective medium theory has been employed. We have shown many different factors to maintain plasmon resonance peaks in NIR region, such as porosity, silver core and surface defects etc. Later, HGNS has been coated with PEG to stabilize its behavior under laser irradiation. Nevertheless, after Ag/Au aspect ratios has been measured at different organs, we concluded silver core in HGNS fragmented into small pieces and was very harmful and toxic for biological application. Later, Bruggeman effective medium theory has also been applied to

hollow gold-cobalt nanoshells and we found tremendous damping effects of cobalt, which has potential application in hot electron generation.

Chapter 5

Conclusion

In my thesis, two major numerical techniques have been employed: one is FEM and the other is FDTD. Both of them are very important methods in plasmonics and nano-photonics research area.

Firstly, we have developed a new numerical method to calculate EELS spectra based on FDTD. Detailed principles and implementation procedures have been provided. Starting with the simplest gold sphere in vacuum case, it shows an excellent agreement between FDTD and BEM results. Then we extended to more complex cases such as silver dimer, gold disk on silicon nitride substrate, bowtie antenna on supported substrates and high density of Ag-Ag dimer. All of those calculations based on FDTD show an excellent agreement with BEM. For some specific strongly coupling geometries, EELS maps have also provided to further help us to

understand different plasmon modes. Our FDTD results also agree well with experimental EELS spectra.

Next, we introduced a quite novel fabrication technique called stretchable colloidal lithography (SCL). Based on this technique, we could create SRRs in a large and identical scale. Optical spectra have been measured in the experiment and numerical calculations based on FEM have confirmed plasmon resonance peaks' locations. Charge plots based on Guass' theorem are obtained. Furthermore, with the aid of standing-wave model, we could understand different plasmon modes' nature. SRRs have wide application in metamaterials and sensors area.

Finally, we discussed HGNS' application in biomedical area. HGNS with size sub-100 nm could be treated as an efficient nanoparticle for cancer therapy since their resonance peak was in NIR region. Detailed chemical synthesis process had been discussed to get HGNS. In order to know the specific composites in HGNS and why the resonance peak was at NIR region independent of particle's sizes, we performed accurate FEM calculations to get extinction cross section spectra. In this process, Bruggeman effective medium theory was used to calculate the dielectric function with a mixture of gold, silver and water at different percentages. Later, laser test showed HGNS would be more stable coated with PEG. However, HGNS fragmented into pieces *in vivo*. Meantime, we found cobalt's surprising damping effects via experiment and Mie theory calculations.

References

1. Ritchie, R. H. Plasma losses by fast eletrons in thin films. *Phys. Rev.* **106,** 874–881 (1957).

2. Powell, C. J. & Swan, J. B. Origin of the characteristic electron energy losses in aluminum. *Phys. Rev.* **115,** 869–875 (1959).

3. Pettit, R. B., Silcox, J. & Vincent, R. Measurement of surface-plasmon dispersion in oxidized aluminum films. *Phys. Rev. B* **11,** 3116–3123 (1975).

4. García De Abajo, F. J. Optical excitations in electron microscopy. *Rev. Mod. Phys.* **82,** 209–275 (2010).

5. García De Abajo, F. J. & Kociak, M. Probing the photonic local density of states with electron energy loss spectroscopy. *Phys. Rev. Lett.* **100,** 1–4 (2008).

6. Asenjo-Garcia, A. & García De Abajo, F. J. Electron energy-gain spectroscopy. *New J. Phys.* **15,** (2013).

7. Kociak, M. & Stéphan, O. Mapping plasmons at the nanometer scale in an electron microscope. *Chem. Soc. Rev.* **43,** 3865–83 (2014).

8. Koh, A. L. *et al.* Electron energy-loss spectroscopy (EELS) of surface plasmons in single silver nanoparticles and dimers: Influence of beam damage and mapping of dark modes. *ACS Nano* **3,** 3015–3022 (2009).

9. Duan, H., Fernandez, A., Bosman, M., Maier, S. a & Yang, J. K. W. Nanoplasmonics : Classical down to the Nanometer Scale. *Nano Lett.* **12,** 1683–1689 (2012).

10. Barrow, S. J., Rossouw, D., Funston, A. M., Botton, G. a. & Mulvaney, P. Mapping bright and dark modes in gold nanoparticle chains using electron energy loss spectroscopy. *Nano Lett.* **14,** 3799–3808 (2014).

11. García de Abajo, F. & Howie, a. Retarded field calculation of electron energy loss in inhomogeneous dielectrics. *Phys. Rev. B* **65,** 1–17 (2002).

12. Talebi, N., Sigle, W., Vogelgesang, R. & Van Aken, P. Numerical simulations of interference effects in photon-assisted electron energy-loss spectroscopy. *New J. Phys.* **15,** (2013).

13. Bigelow, N. W., Vaschillo, A., Iberi, V., Camden, J. P. & Masiello, D. J. Characterization of the electron- and photon-driven plasmonic excitations of metal nanorods. *ACS Nano* **6,** 7497–7504 (2012).

14. Bigelow, N. W., Vaschillo, A., Camden, J. P. & Masiello, D. J. Signatures of fano interferences in the electron energy loss spectroscopy and cathodoluminescence of symmetry-broken nanorod dimers. *ACS Nano* **7,** 4511–4519 (2013).

15. Reed, B., Chen, J., MacDonald, N., Silcox, J. & Bertsch, G. Fabrication and STEM/EELS measurements of nanometer-scale silicon tips and filaments. *Phys. Rev. B* **60,** 5641–5652 (1999).

16. Song, F. *et al.* Visualizing plasmon coupling in closely spaced chains of Ag nanoparticles by electron energy-loss spectroscopy. *Small* **6,** 446–451 (2010).

17. Scholl, J. a., Koh, A. L. & Dionne, J. a. Quantum plasmon resonances of individual metallic nanoparticles. *Nature* **483,** 421–427 (2012).

18. Cao, Y., Manjavacas, A., Large, N. & Nordlander, P. Electron Energy-Loss Spectroscopy Calculation in Finite-Difference Time-Domain Package. *ACS Photonics* **2,** 369–375 (2015).

19. Lumerical Solutions, I. No Title. at <http://www.lumerical.com/tcad-products/fdtd/>

20. Novotny, L. & Hecht, B. *Principles of Nano-Optics*. (Cambridge University Press: New York, 2006).

21. Jackson, J. *Classical Electrodynamics*. (Wiley, 1998).

22. Bérenger, J.-P. *Perfectly Matched Layer (PML) for Computational Electromagnetics*. *Synthesis Lectures on Computational Electromagnetics* **2,** (2007).

23. Johnson, P. . & Christy, R. W. Optical Constants of the Noble Metals. *Phys. Rev. B* **6,** 4370–4379 (1972).

24. Palik, E. D. *Handbook of Optical Constants of Solids*. (Academic Press: New York, 1985).

25. García de Abajo, F. & Howie, a. Relativistic Electron Energy Loss and Electron-Induced Photon Emission in Inhomogeneous Dielectrics. *Phys. Rev. Lett.* **80,** 5180–5183 (1998).

26. Matyssek, C., Niegemann, J., Hergert, W. & Busch, K. Computing electron energy loss spectra with the Discontinuous Galerkin Time-Domain method. *Photonics Nanostructures - Fundam. Appl.* **9,** 367–373 (2011).

27. Kadkhodazadeh, S., Wagner, J. B., Kneipp, H. & Kneipp, K. Coexistence of classical and quantum plasmonics in large plasmonic structures with subnanometer gaps. *Appl. Phys. Lett.* **103,** 2011–2015 (2013).

28. Kadkhodazadeh, S. *et al.* Scaling of the surface plasmon resonance in gold and silver dimers probed by EELS. *J. Phys. Chem. C* **118,** 5478–5485 (2014).

29. Nordlander, P., Oubre, C., Prodan, E., Li, K. & Stockman, M. I. Plasmon hybridization in nanoparticle dimers. *Nano Lett.* **4,** 899–903 (2004).

30. Prodan, E. & Nordlander, P. Plasmon hybridization in spherical nanoparticles. *J. Chem. Phys.* **120,** 5444–5454 (2004).

31. Knight, M. W., Wu, Y., Lassiter, J. B., Nordlander, P. & Halas, N. J. Substrates matter: influence of an adjacent dielectric on an individual plasmonic nanoparticle. *Nano Lett.* **9,** 2188–2192 (2009).

32. Bååk, T. Silicon oxynitride; a material for GRIN optics. *Appl. Opt.* **21,** 1069–1072 (1982).

33. Philipp, H. R. Optical Properties of Silicon Nitride. *J. Electrochem. Soc.* **120,** 295 (1973).

34. Tanaka, M., Saida, S. & Tsunashima, Y. Film Properties of Low-k Silicon Nitride Films Formed by Hexachlorodisilane and Ammonia. *J. Electrochem. Soc.* **147,** 2284 (2000).

35. Koh, A. L., Fernández-Domínguez, A. I., McComb, D. W., Maier, S. a. & Yang, J. K. W. High-resolution mapping of electron-beam-excited plasmon modes in lithographically defined gold nanostructures. *Nano Lett.* **11,** 1323–1330 (2011).

36. Zhang, M. *et al.* High-density 2D homo- and hetero- plasmonic dimers with universal sub-10-nm gaps. *Nat. Commun.*

37. Large, N. *et al.* Plasmonic properties of gold ring-disk nano-resonators: fine shape details matter. *Opt. Express* **19,** 5587–5595 (2011).

38. Shelby, R. a, Smith, D. R. & Schultz, S. Experimental verification of a negative index of refraction. *Science* **292,** 77–79 (2001).

39. Luk'yanchuk, B. *et al.* The Fano resonance in plasmonic nanostructures and metamaterials. *Nat. Mater.* **9,** 707–715 (2010).

40. Zheludev, N. I. Applied physics. The road ahead for metamaterials. *Science* **328,** 582–583 (2010).

41. Pendry, J. B., Holden, a. J., Robbins, D. J. & Stewart, W. J. Magnetism from conductors and enhanced nonlinear phenomena. *IEEE Trans. Microw. Theory Tech.* **47,** 2075–2084 (1999).

42. Xie, Q. *et al.* Fabrication of nanostructures with laser interference lithography. *J. Alloys Compd.* **449,** 261–264 (2008).

43. Lin, Y. *et al.* Ultrafast-laser-induced parallel phase-change nanolithography. *Appl. Phys. Lett.* **89,** 21–24 (2006).

44. Gao, L. *et al.* Fabrication of split-ring resonators by tilted nanoimprint lithography. *J. Colloid Interface Sci.* **360,** 320–323 (2011).

45. Shumaker-Parry, J. S., Rochholz, H. & Kreiter, M. Fabrication of crescent-shaped optical antennas. *Adv. Mater.* **17,** 2131–2134 (2005).

46. Rochholz, H., Bocchio, N. & Kreiter, M. Tuning resonances on crescent-shaped noble-metal nanoparticles. *New J. Phys.* **9,** (2007).

47. Wu, L. Y., Ross, B. M. & Lee, L. P. Optical properties of the crescent-shaped nanohole antenna. *Nano Lett.* **9,** 1956–1961 (2009).

48. Vogel, N. *et al.* Plasmon hybridization in stacked double crescents arrays fabricated by colloidal lithography. *Nano Lett.* **11,** 446–454 (2011).

49. Cataldo, S. *et al.* Hole-mask colloidal nanolithography for large-area low-cost metamaterials and antenna-assisted surface-enhanced infrared absorption substrates. *ACS Nano* **6,** 979–985 (2012).

50. Cai, Y., Zhao, Z., Chen, J., Yang, T. & Cremer, P. S. Deflected Capillary Force Lithography. *ACS Nano* **6,** 1548–1556 (2012).

51. Cai, Y., Cao, Y., Nordlander, P. & Cremer, P. S. Fabrication of Split-Rings via Stretchable Colloidal Lithography. *ACS Photonics* **1,** 127–134 (2014).

52. Cai, Y., Li, Y., Nordlander, P. & Cremer, P. S. Fabrication of elliptical nanorings with highly tunable and multiple plasmonic resonances. *Nano Lett.* **12,** 4881–4888 (2012).

53. Bruinink, C. M. *et al.* Capillary force lithography: Fabrication of functional polymer templates as versatile tools for nanolithography. *Adv. Funct. Mater.* **16,** 1555–1565 (2006).

54. Lee, S. Y., Jeong, J. R., Kim, S. H., Kim, S. & Yang, S. M. Arrays of ferromagnetic nanorings with variable thickness fabricated by capillary force lithography. *Langmuir* **25,** 12535–12540 (2009).

55. Zheng, Y. B., Juluri, B. K., Mao, X., Walker, T. R. & Huang, T. J. Systematic investigation of localized surface plasmon resonance of long-range ordered Au nanodisk arrays. *J. Appl. Phys.* **103,** (2008).

56. Zheng, Y. B. & Huang, T. J. Thermal behavior of localized surface plasmon resonance of Au/TiO2 core/shell nanoparticle arrays. *Appl. Phys. Lett.* **90,** 183117 (2007).

57. Bocchio, N. L., Unger, A., Alvarez, M. & Kreiter, M. Thin layer sensing with multipolar plasmonic resonances. *J. Phys. Chem. C* **112,** 14355–14359 (2008).

58. Chen, C. Y., Wu, S. C. & Yen, T. J. Experimental verification of standing-wave plasmonic resonances in split-ring resonators. *Appl. Phys. Lett.* **93,** 2006–2009 (2008).

59. Nordlander, P. The Ring: A leitmotif in plasmonics. *ACS Nano* **3,** 488–492 (2009).

60. Xu, Q. *et al.* Fabrication of large-area patterned nanostructures for optical applications by nanoskiving. *Nano Lett.* **7,** 2800–2805 (2007).

61. Neubrech, F. *et al.* Resonances of individual metal nanowires in the infrared. *Appl. Phys. Lett.* **89,** 2004–2007 (2006).

62. Bardhan, R. *et al.* Nanoshells with targeted simultaneous enhancement of magnetic and optical imaging and photothermal therapeutic response. *Adv. Funct. Mater.* **19,** 3901–3909 (2009).

63. Bardhan, R. *et al.* Tracking of multimodal therapeutic nanocomplexes targeting breast cancer in vivo. *Nano Lett.* **10,** 4920–4928 (2010).

64. Bardhan, R., Lal, S., Joshi, A. & Halas, N. J. Imaging and Treatment of Cancer. *Acc. Chem. Res.* **44,** 936–946 (2011).

65. Weissleder, R. A clearer vision for in vivo imaging Progress continues in the development of smaller , more penetrable probes for biological imaging. *Nat. Biotechnol.* **19,** 316–317 (2001).

66. Dickerson, E. B. *et al.* Gold nanorod assisted near-infrared plasmonic photothermal therapy (PPTT) of squamous cell carcinoma in mice. *Cancer Lett.* **269,** 57–66 (2008).

67. Goodrich, G. P. *et al.* Photothermal therapy in a murine colon cancer model using near-infrared absorbing gold nanorods. *J. Biomed. Opt.* **15,** 018001 (2010).

68. Huang, X., El-Sayed, I. H., Qian, W. & El-Sayed, M. a. Cancer cell imaging and photothermal therapy in the near-infrared region by using gold nanorods. *J. Am. Chem. Soc.* **128,** 2115–2120 (2006).

69. Chen, J. *et al.* Immuno gold nanocages with tailored optical properties for targeted photothermal destruction of cancer cells. *Nano Lett.* **7,** 1318–1322 (2007).

70. Chen, W. *et al.* A molecularly targeted theranostic probe for ovarian cancer. *Mol. Cancer Ther.* **9,** 1028–1038 (2010).

71. Melancon, M. P. *et al.* In vitro and in vivo targeting of hollow gold nanoshells directed at epidermal growth factor receptor for photothermal ablation therapy. *Mol. Cancer Ther.* **7,** 1730–1739 (2008).

72. Lu, W. *et al.* Effects of photoacoustic imaging and photothermal ablation therapy mediated by targeted hollow gold nanospheres in an orthotopic mouse xenograft model of glioma. *Cancer Res.* **71,** 6116–6121 (2011).

73. Wang, S.-H., Lee, C.-W., Chiou, A. & Wei, P.-K. Size-dependent endocytosis of gold nanoparticles studied by three-dimensional mapping of plasmonic scattering images. *J. Nanobiotechnology* **8,** 33 (2010).

74. An, K. & Hyeon, T. Synthesis and biomedical applications of hollow nanostructures. *Nano Today* **4,** 359–373 (2009).

75. Choi, Y., Hong, S., Liu, L., Kim, S. K. & Park, S. Galvanically replaced hollow Au-Ag nanospheres: Study of their surface plasmon resonance. *Langmuir* **28,** 6670–6676 (2012).

76. Lu, X., Chen, J., Skrabalak, S. E. & Xia, Y. Galvanic replacement reaction: a simple and powerful route to hollow and porous metal nanostructures. *Proc. Inst. Mech. Eng. Part N J. Nanoeng. Nanosyst.* **221,** 1–16 (2008).

77. Preciado-Flores, S. *et al.* Highly reproducible synthesis of hollow gold nanospheres with near infrared surface plasmon absorption using PVP as stabilizing agent. *J. Mater. Chem.* **21,** 2344 (2011).

78. Schwartzberg, A. M., Olson, T. Y., Talley, C. E. & Zhang, J. Z. Synthesis, characterization, and tunable optical properties of hollow gold nanospheres. *J. Phys. Chem. B* **110,** 19935–19944 (2006).

79. Sun, Y. & Xia, Y. Mechanistic Study on the Replacement Reaction between Silver Nanostructures and Chloroauric Acid in Aqueous Medium Mechanistic Study on the Replacement Reaction between Silver Nanostructures and Chloroauric Acid in Aqueous. 3892–3901 (2004). doi:10.1021/ja039734c

80. Sun, Y., Mayers, B. T. & Xia, Y. Template-Engaged Replacement Reaction: A One-Step Approach to the Large-Scale Synthesis of Metal Nanostructures with Hollow Interiors. *Nano Lett.* **2,** 481–485 (2002).

81. Wang, W., Dahl, M. & Yin, Y. Hollow nanocrystals through the nanoscale Kirkendall effect. *Chem. Mater.* **25,** 1179–1189 (2013).

82. Goodman, A. M. *et al.* The surprising in vivo instability of near-IR-absorbing hollow Au-Ag nanoshells. *ACS Nano* **8,** 3222–3231 (2014).

83. Zeng, X. C., Bergman, D. J., Hui, P. M. & Stroud, D. Effective-medium theory for weakly nonlinear composites. *Phys. Rev. B* **38,** 10970–10973 (1988).

84. Shi, Z. *et al.* Surface-plasmon polaritons on metal-dielectric nanocomposite films. *Opt. Lett.* **34,** 3535–3537 (2009).

85. Lipka, J. *et al.* Biodistribution of PEG-modified gold nanoparticles following intratracheal instillation and intravenous injection. *Biomaterials* **31,** 6574–6581 (2010).

86. Gomes-Da-Silva, L. C. *et al.* Lipid-based nanoparticles for siRNA delivery in cancer therapy: Paradigms and challenges. *Acc. Chem. Res.* **45,** 1163–1171 (2012).

87. Rao, J. Shedding light on tumors using nanoparticles. *ACS Nano* **2,** 1984–1986 (2008).

88. Kittler, S., Greulich, C., Diendorf, J., Köller, M. & Epple, M. Toxicity of silver nanoparticles increases during storage because of slow dissolution under release of silver ions. *Chem. Mater.* **22,** 4548–4554 (2010).

89. Xiu, Z., Zhang, Q., Puppala, H. L., Colvin, V. L. & Alvarez, P. J. J. Negligible Particle-Speci fi c Antibacterial Activity of Silver Nanoparticles. *Nano Lett.* **12,** 4271–4275 (2012).

90. Thibodeaux, C. a *et al.* Impurity-Induced Plasmon Damping in Individual Cobalt-Doped Hollow Au Nanoshells. *J. Phys. Chem. B* (2014). doi:10.1021/jp504467j
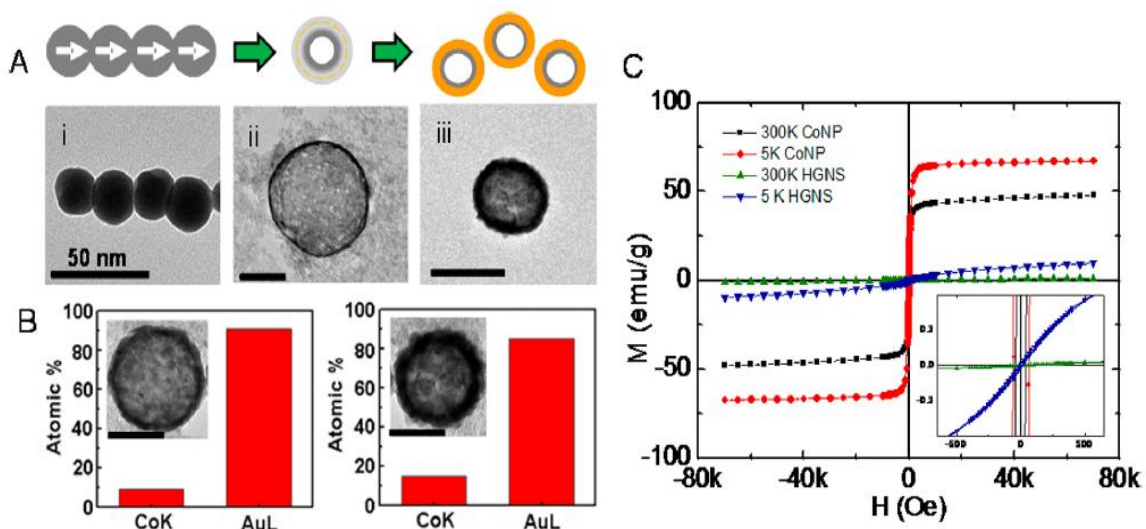
Appendix

Figure S1: Synthesis of Hollow gold-cobalt nanoshell and its magnetization
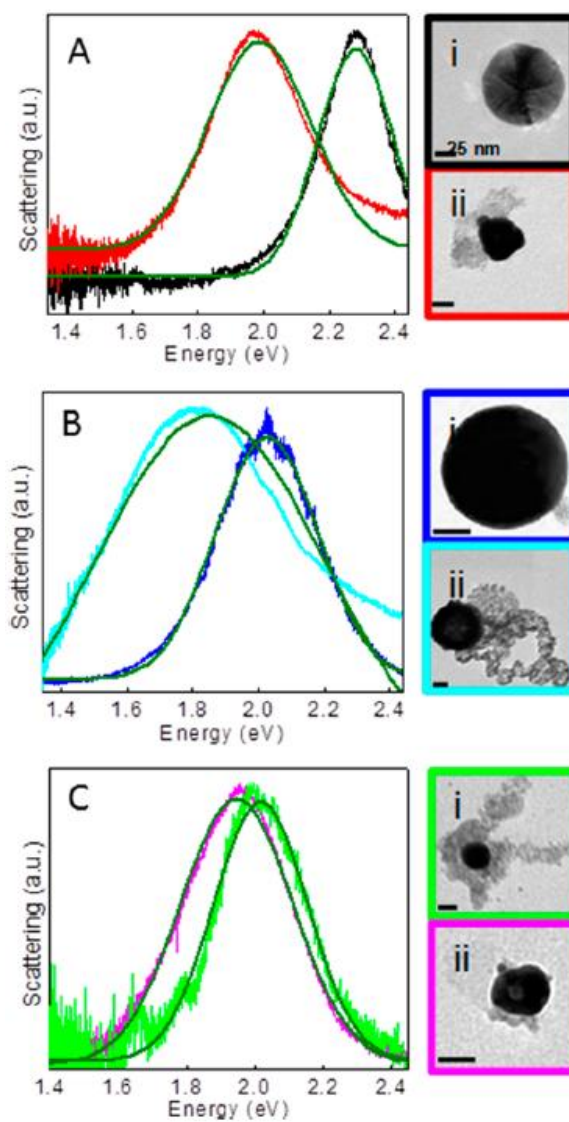
properties

Figure S2: Experimental scattering for different sizes (35 nm, 50 nm, 100 nm) Co-HGNS and colloid gold